Research Square

Preprints are preliminary reports that have not undergone peer review.
They should not be considered conclusive, used to inform clinical practice,
or referenced by the media as validated information.

A novel bispecific adaptor platform enhances CD19-CAR T cell persistence and efficacy in solid tumors

Clare slaney

clare.slaney@petermac.org

Peter MacCallum Cancer Centre https://orcid.org/0000-0002-6986-6115

Rachel Xu

Peter MacCallum Cancer Centre https://orcid.org/0000-0002-6178-1854

Yuchen Bai

University of Melbourne https://orcid.org/0000-0002-3389-7104

Yao Wang

The University of Sydney

Lining Ju

The University of Sydney https://orcid.org/0000-0002-7591-0864

Jasmine Jin

The University of Sydney

Haoqing Wang

The University of Sydney

Bianca von Scheidt

Peter MacCallum Cancer Centre

Xiaomeng Zhang

Peter MacCallum Cancer Centre

Dmitry Zorin

Peter MacCallum Cancer Centre

Olivia Hidajat

Peter MacCallum Cancer Centre

Ruihong Huang

Peter MacCallum Cancer Centre

Evan Pappas

Peter MacCallum Cancer Centre

Brian Liddicoat

Peter MacCallum Cancer Centre

Charbel Darido

Peter MacCallum Cancer Centre https://orcid.org/0000-0002-6541-324X
Paul Neeson
Peter MacCallum Cancer Centre https://orcid.org/0000-0002-2729-5887
Joseph Trapani
Peter MacCallum Cancer Center
Michael Kershaw
Peter MacCallum Cancer Centre
Michael Dickinson
Peter MacCallum Cancer Centre https://orcid.org/0000-0002-1492-5966
Phillip Darcy
Peter MacCallum Cancer Centre https://orcid.org/0000-0002-5303-9561
Jie Sun
Zhejiang University https://orcid.org/0000-0002-5642-0560
Christine Ambrose
Aleta Biotherapeutics
Paul Rennert
Aleta Biotherapeutics

Article

Keywords: chimeric antigen receptor (CAR), solid tumors, CD19, bispecifics, avidity

Posted Date: November 17th, 2026

DOI: https://doi.org/10.21203/rs.3.rs-11591978/v1

License: This work is licensed under a Creative Commons Attribution 4.0 International License.
Read Full License

Additional Declarations: Yes there is potential Competing Interest. CS, BvS and MHK are scientific founders of Currus Biologics. PR is the CSO and CA is a PI of Aleta Bio.

A novel bispecific Adaptor platform enhances CD19-CAR T cell persistence and efficacy in solid tumors

Rachel Xu[1,2], Yuchen Bai[1,2], Yao Wang[3,4], Bianca von Scheidt[1], Xiaomeng Zhang[1,2], Ruihong Huang[1,2], Dmitry Zorin[1], Olivia Hidajat[1,2], Evan G. Pappas[1,2], Brian J. Liddicoat[1], Jasmine Jin[3], Haoqing J. Wang[3,4,6], Charbel Darido[1,2], Jie Sun[5], Joseph A. Trapani[1,2], Paul J. Neeson[1,2], Michael Dickinson[1,2], Christine Ambrose[7], Paul D. Rennert[7], Lining Arnold Ju[3,4,6], Michael H. Kershaw[1,2], Phillip K. Darcy[1,2*] and Clare Y. Slaney[1,2*]

[1]Peter MacCallum Cancer Centre, Melbourne, Victoria 3000, Australia.
[2]Sir Peter MacCallum Department of Oncology, The University of Melbourne, Parkville, Victoria 3010, Australia.
[3]School of Biomedical Engineering, The University of Sydney, Darlington, New South Wales 2008, Australia.
[4]Charles Perkins Centre, The University of Sydney, Camperdown, New South Wales 2006, Australia.
[5]Department of Cell Biology, Zhejiang University School of Medicine, Zhejiang University, Hangzhou 310058, China.
[6]Heart Research Institute, Newtown, New South Wales 2042, Australia.
[7]Aleta Biotherapeutics, Natick, Massachusetts 01760, United States of America.

*Address correspondence to Clare Y. Slaney (clare.slaney@petermac.org) or Phillip K. Darcy (phil.darcy@petermac.org).

Abstract

Chimeric antigen receptor (CAR) T cell therapy has transformed hematological cancer treatment but remains ineffective in solid tumors. Here, we compared CD19-CAR and HER2-CAR T cells with identical backbones in matched tumor models. Strikingly, CD19-CAR T cells eradicated all tested $CD19^+$ solid tumors *in vivo*, whereas HER2-CAR T cells failed to control matched $HER2^+$ solid tumors. Superior CD19-CAR efficacy was associated with greater avidity, stronger signaling, and rapid degranulation. To harness these favorable properties for solid tumor treatment, we developed and compared bispecific Adaptors redirecting CD19-CAR T cell activity against $HER2^+$ cancers. Our lead nanobody-based Adaptor 4 incorporating an albumin-binding VHH improves upon earlier designs by enhancing manufacturability and tumor infiltration while retaining systemic persistence. It induced complete tumor regression and prolonged survival in two solid tumor models. Mechanistically, Adaptor 4 enhanced CAR T cell-tumor cell engagement, signaling and intratumoral infiltration, accompanied by spatially distinct CAR T cell states and local inflammatory remodeling. Long-term tumor-free mice rejected tumor rechallenge, demonstrating durable antitumor protection. Importantly, Adaptor 4 remained effective when combined with CD19-CAR T cells generated from patients with advanced solid cancers. Together, these findings establish an enhanced Adaptor strategy redirecting clinically validated CD19-CAR T cells for solid tumor treatment.

Key words

chimeric antigen receptor (CAR), solid tumors, CD19, bispecifics, avidity.

Running title

Adaptor-mediated CAR T Cells Therapy for Solid Tumors

Introduction

Adoptive cell therapies, including chimeric antigen receptor (CAR) T cell therapies, have significantly advanced cancer treatment. CAR T cells are generated by genetically modifying patient T cells to express a CAR, which enables T cells to recognize cancer antigens and trigger T cell activation and cytotoxicity. This approach has demonstrated remarkable clinical efficacy, particularly in B-cell malignancies. To date, seven CAR T cell therapies have been approved by the US Food and Drug Administration (FDA): five targeting the B-cell lineage marker CD19 and two targeting B-cell maturation antigen (BCMA), all in the treatment of hematologic cancers[1,2].

In contrast, CAR T cell therapy has shown limited efficacy against solid tumors despite extensive evaluation of diverse target antigens[3]. Multiple factors are believed to contribute to the limited efficacy, including the immunosuppressive tumor microenvironment (TME), antigen heterogeneity, and insufficient CAR T cell trafficking and infiltration[3-5]. However, the contribution of the CAR-antigen interaction itself remains less well understood. Differences in cancer type, CAR design and manufacturing make clinical comparisons difficult, while preclinical studies have generally evaluated individual CARs in distinct cancer models[6,7]. Consequently, the extent to which CAR-antigen interactions influence the therapeutic efficacy remains poorly defined.

Here we generated CD19-CAR and HER2-CAR T cells with identical backbones and directly compared their treatment efficacies in matched cancer models. CD19-CAR T cells consistently outperformed HER2-CAR T cells in matched solid tumor models, despite comparable activity in conventional *in vitro* assays. Superior CD19-CAR activity was associated with greater cellular avidity, stronger proximal CAR signaling and more rapid degranulation. We therefore sought to develop a strategy to redirect CD19-CAR T cells against $HER2^+$ solid tumors, aiming to harness the favorable functional properties of CD19-CAR T cells for solid tumor treatment.

Several strategies have previously been developed to redirect CD19-CAR T cells against solid tumors[8-12]. Examples include CD19-CAR T cells modified to constitutively secrete CD19-anti-HER2 bispecific proteins, which demonstrated anti-tumor efficacy at the expense of more complex CAR engineering[10]. In contrast, Hombach *et al.* reported only modest suppression of $HER2^+$ tumor growth using a purified CD19-anti-HER2 recombinant engager, without

demonstrating complete tumor regression or reporting long-term survival outcomes[11]. While these studies establish the feasibility of CD19-CAR redirection, the mechanisms governing effective CAR T cell engagement and the contributions of bispecific protein design, systemic persistence and tumor penetration to therapeutic efficacy remain poorly understood. In this study, we developed a novel recombinant Adaptor platform with sufficient serum persistence to support CAR T cell function while promoting deeper tumor infiltration. In addition, the platform could be readily combined with clinically established CD19-CAR T cells, without additional genetic engineering required.

We iteratively optimized the Adaptor design to improve manufacturability, maintain sufficient serum persistence and enhance tumor penetration. The lead candidate, Adaptor 4, was a compact VHH-based molecule incorporating an albumin-binding VHH to support serum persistence. Adaptor 4 induced substantial tumor regression and prolonged survival across two solid cancer xenograft models, including complete tumor clearance in the majority of treated mice and up to 100 days of tumor-free survival. This robust therapeutic efficacy was associated with stronger CAR T cell-tumor cell engagement, increased CAR signaling, and deeper intratumoral infiltration. Anti-tumor responses mediated by Adaptor 4 were associated with spatially distinct CAR T cell states and local inflammatory remodeling. Long-term tumor-free mice retained detectable CAR T cells and rejected tumor rechallenge following Adaptor 4 re-administration. Notably, Adaptor 4 remained effective with CD19-CAR T cells generated from patients with advanced solid cancers, supporting its strong translational potential. Together, these findings establish a significantly improved bispecific Adaptor strategy for extending the efficacy of CD19-CAR T cells to solid cancers.

Results

CD19-CAR T cells demonstrate superior efficacy in matched solid tumors models.

To directly compare CARs used for hematologic and solid cancers, we generated CD19- and HER2-CAR T cells with identical second-generation CD28-CD3ζ backbones, differing only in their single chain variable fragments (scFvs) (**Supplementary Figure 1a)**. Across multiple donors, both CAR T cells showed comparable transduction rates, CD4:CD8 ratios, memory phenotypes, exhaustion marker expression and expansion kinetics (**Supplementary Figure 1b-f**). Both also demonstrated robust antigen-dependent cytotoxicity and IFN-γ production against respective target cells *in vitro* **(Figure 1a-d**).

Consistent with their established clinical performances[4,13], CD19-CAR T cells efficiently controlled NALM6 leukemia *in vivo*, whereas HER2-CAR T cells showed limited activity against MDA-MB-468-HER2 solid tumors, even at substantially higher cell doses (**Supplementary Figure 2a-b**). We therefore asked whether this disparity reflected intrinsic differences within the tumor models or perhaps related to the CAR-antigen interactions, irrespective of the disease model.

To address this, we generated matched NALM6 and MDA-MB-468 tumor models with comparable CD19 or HER2 expression, and CD19- and HER2-CAR T cells with similar levels of surface CAR expression (**Supplementary Figure 3a-b**). CD19-CAR T cells rapidly controlled and eradicated NALM6-CD19, MDA-MB-468-CD19 and SKOV3-CD19 tumors engrafted in NSG mice (**Figure 1e-g**). In striking contrast, HER2-CAR T cells failed to control the corresponding $HER2^{+}$ xenograft tumors (**Figure 1h-j**), and this lack of efficacy could not be overcome by simply increasing the number of adoptively transferred HER2-CAR T cells (**Supplementary Figure 2b and Figure 1j**).

Immunohistochemistry (IHC) and flow cytometry analyses demonstrated substantially greater abundance of CD19-CAR T cells than HER2-CAR T cells in the tumors (**Figure 1k-l)**. Thus, across three distinct solid tumor models, CD19-CAR T cells consistently exhibited markedly greater *in vivo* activity than HER2-CAR T cells generated using the same backbone and donor T cells. These findings suggest that the CAR-antigen interaction itself may be a major determinant of CAR T cell outcomes in solid tumors, irrespective of cancer type.

CD19-CAR T cells show better target cell engagement, signaling, and activation.

Given the markedly better antitumor activity of CD19-CAR T cells in solid tumors, we investigated whether they interacted more effectively with their target cells than HER2-CAR T cells. To achieve this, we used lattice light-sheet-based high resolution fluorescence microscopy[14] to capture 3D live-cell interactions over time. The technology revealed larger and longer-lasting immunological synapses formed between CD19-CAR T cells and NALM6-CD19 cells than those formed between HER2-CAR T cells and NALM6-HER2 cells (**Figure 2a-b**), suggesting potentially stronger biophysical interactions. To measure the mechanical strength of these interactions, we utilized z-Movi platform-based acoustic force spectroscopy,

where a monolayer of target cancer cells adhered onto specialized microfluidic chips were subsequently incubated with CAR T cells, and the proportion of remaining bound cells was measured against lifting acoustic forces. Using this technology, we observed that significantly more CD19-CAR T cells remained bound to their target cells as increasing forces was applied, demonstrating stronger overall cellular avidity than HER2-CAR T cells (**Figure 2c**). Consistent with this enhanced target cell engagement, CD19-CAR T cells exhibited increased phosphorylation of ZAP70 and ERK1/2 and greater CD107a mobilization upon antigen encounter (**Figure 2d-f**), suggesting stronger proximal signaling and more rapid degranulation. Such observations fit a previously described model whereby stronger mechanical forces from target antigen engagement induced an increase in contact area sizes, CAR micro cluster formation, and CAR signaling[15].

We next examined whether these functional differences were reflected in tumor-experienced CAR T cells *in vivo*. Bulk RNA sequencing of CD19- and HER2-CAR T cells isolated from matched solid tumors revealed distinct transcriptional profiles. Intra-tumoral CD19-CAR T cells showed increased expression of genes associated with cytotoxic effector function, including GZMA, GZMB, GZMK, as well as genes involved in T cell signaling, including PIK3CA, PIK3CB, MAP3K8, MAP3K20, STAT1, and IL2RG. Genes associated with cell adhesion and cytoskeleton organization, including ADAM17, ITGA1, ITGB2 and ACTB (F-actin) were also elevated. In addition, several genes associated with T cell homeostasis and memory, including SELL, IL7R, FOXO3 and ILF2, were more highly expressed in CD19-CAR T cells (**Figure 2g**). Consistent with these data, gene set enrichment analysis showed that CD19-CAR T cells were enriched for pathways associated with cytoskeleton organization, cell migration and signaling, whereas HER2-CAR T cells showed enrichment of metabolic and mitochondrial programs and pathways associated with negative regulation of cytokine and type II interferon responses (**Figure 2h**). Together, these data indicate that CD19-CAR T cells adopt a transcriptional state consistent with enhanced target-cell engagement and effector function within solid tumors.

We then asked whether the functional advantage of CD19-CAR T cells observed in solid tumor extended to blood cancers. In contrast to the marked disparity observed in solid tumors, both CD19- and HER2-CAR T cells effectively suppressed antigen-matched NALM6 leukemia *in vivo* and showed comparable activity against NALM6 cells *in vitro* (**Supplementary Figure**

4a-c). We asked whether this reflected a greater intrinsic susceptibility of NALM6 cells to CAR T cell-mediated killing. Indeed, NALM6 cells were more readily killed than MDA-MB-468 cells *in vitro* (**Supplementary Figure 4d-e**), despite inducing less IFN-γ production in CAR T cells (**Supplementary Figure 4f-g**). CAR T cell cytotoxicity was dependent on perforin/granzyme B-mediated apoptosis, as confirmed by the abrogation of killing in the presence of EGTA, a calcium chelator preventing perforin pore formation and granzyme delivery (**Supplementary Figure 5a**). We therefore investigated whether the differential killing reflected intrinsic differences in apoptotic sensitivity between NALM6 cells and MDA-MB-468 cells. Examination of public RNA/protein, RNAi, CRISPR, and drug-sensitivity datasets collectively indicated that NALM6 cells were more prone to apoptosis than MDA-MB-468 cells (**Supplementary Figure 5b-d**). We further examined differences in apoptotic programs and found that apoptosis-associated transcriptional programs were strongly enriched in B-lymphoblastic leukemia/lymphoma than in invasive breast cancers (**Supplementary Figure 5e-h**). Together, these findings indicate that NALM6 leukemia cells are more susceptible to apoptosis and are therefore more sensitive to CAR T cell-mediated apoptosis than MDA-MB-468 solid tumor cells. Thus, high-quality CAR-target engagement may become particularly important when targeting relatively resistant solid tumor cells.

Adaptors redirect CD19-CAR T cells to target HER2$^+$ tumors

Given the superior anti-tumor efficacy of CD19-CAR T cells, we sought to harness their potent activity for HER2$^+$ solid tumors. We developed a series of three different recombinant bispecific Adaptor reagents containing the human CD19 extracellular domain (ECD) linked to an anti-HER2 scFv (**Figure 3a**). Conceptually related CD19-CAR T cell redirection strategies have previously demonstrated the feasibility of redirecting CD19-CAR T cells toward HER2$^+$ tumors[10,11], but did not demonstrate superior therapeutic efficacy over conventional HER2-CAR T cells. In particular, Hombach et al. using purified CD19-anti-HER2 proteins achieved only modest *in vivo* efficacy, yet pharmacokinetics and alternative dosing regimens were not evaluated. We consequently generated Adaptor 1 containing the full-length CD19-ECD, Adaptor 2 incorporating a 15-amino acid C-terminal truncation to improve protein expression, and Adaptor 3 additionally incorporating a PGLALA-mutated human IgG1 Fc domain to prolong serum half-life through neonatal Fc receptor (FcRn) recycling while avoiding cellular degradation through Fc receptor binding[16] (**Figure 3b**).

All three Adaptor formats specifically bound to both CD19-CAR T cells and HER2$^+$ cancer cells (**Figure 3c**) and redirected CD19-CAR T cells to kill HER2$^+$ cancer cells and secrete IFN-γ *in vitro* (**Figure 3d-e**). Soluble Adaptors alone did not activate CAR T cells in the absence of tumor cells (**Supplementary Figure 6a)**, reducing the likelihood of chronic activation induced T cell anergy and dysfunction.

Despite similar *in vitro* activity, the Adaptors differed in protein production characteristics, with Adaptor 1 showing poor yield and Adaptors 2 and 3 being more readily produced (**Figure 3f**). These findings are consistent with CD19-ECD being a well-recognized difficult-to-express protein[17]. As we were unable to produce sufficient Adaptor 1 for *in vivo* studies, and it was therefore not included in downstream experiments. In NSG mice bearing established MDA-MB-468-HER2 mammary tumors, Adaptor 3 effectively redirected CD19-CAR T cells to suppress tumor growth, whereas HER2-CAR T cells, Adaptors alone, CD19-CAR T cells alone, or CD19-CAR T cells combined with Adaptor 2 were ineffective (**Figure 3g**). Notably, treatment was well tolerated, with no detectable loss of body weight (**Supplementary Figure 6b)**.

The difference between Adaptors 2 and 3 was associated with their *in vivo* persistence. Adaptor 2 rapidly declined to undetectable serum levels shortly after injection, whereas Adaptor 3 persisted and remained detectable on HER2$^+$ tumor cells 7 days after treatment (**Figure 3h-i**). Despite the increased efficacy observed, all tumors eventually relapsed. Further analysis by IHC and immunofluorescent (IF) staining showed that both CAR T cell infiltration and Adaptor 3 distribution were confined to the tumor margin, with minimal penetration into the tumor core (**Figure 3j-k**). Xenium-based spatial profiling further showed that the T cell-recruiting chemokine transcripts, CXCL9, CXCL10 and CXCL11, were similarly localized to peripheral tumor regions (**Figure 3l**), indicating a spatially restricted peripheral CAR T cell response and suggesting that limited Adaptor 3 penetration may impede deeper intratumoral CAR T cell responses.

A compact nanobody-based Adaptor 4 enhances CD19-CAR T cell efficacy

To improve Adaptor potency and tumor infiltration while retaining manufacturability and systemic persistence, we developed a more compact nanobody-based Adaptor 4. Here, the full-length CD19 ECD was replaced with a mutagenized CD19 ECD with favorable biophysical

properties including thermostability, protein expression and protease resistance[18]. The anti-HER2 scFv was replaced with a smaller anti-HER2 VHH, and the Fc domain was replaced with a smaller albumin-binding VHH (Alb8) for serum persistence (**Figure 4a**). Despite significantly reducing molecular weight from 170 kDa to 57 kDa, Adaptor 4 retained binding to CD19-CAR T cells and $HER2^+$ cancer cells (**Figure 4b**). It also showed greater activity than Adaptor 3, including enhanced tumor-killing and IFN-γ production *in vitro*, particularly at low concentrations (**Figure 4c-d**). The improved potency translated into a striking therapeutic advantage *in vivo*. In NSG mice bearing MDA-MB-468-HER2 tumors, Adaptor 4 combined with CD19-CAR T cells induced complete tumor regression and durable survival (**Figure 4e-f**), with no associated body weight loss (**Supplementary Figure 6c)**. This was accompanied by substantially greater CAR T cell accumulation in spleens and tumors compared with Adaptor 3 treatment (**Figure 4g-h**). Similar efficacy was observed in an orthotopic MDA-MB-231-HER2 breast cancer xenograft model with complete regression achieved in five-out-of-six mice and prolonged survival (**Figure 4i-j**), with no evidence of body weight loss (**Supplementary Figure 6d)**. In addition, Adaptor 4 remained detectable in serum for several days (**Figure 4k**) and induced deeper T cell infiltration into MDA-MB-468-HER2 tumors (**Figure 4l-m**).

Adaptor 4 enhances CAR T cell engagement, signaling and intratumoral activation

We next investigated the mechanisms underlying the improved activity of Adaptor 4. Lattice light-sheet microscopy revealed that Adaptor 4 promoted more frequent and sustained, multivalent CD19-CAR T cell engagement with tumor cells than Adaptor 3, although we did not observe larger synapses (**Figure 5a-b** and **Supplementary Movie 1-2**). Consistent with this, z-Movi analysis showed stronger CAR T cell-tumor avidity with Adaptor 4 (**Figure 5c**). These findings indicate that the compact Adaptor 4 architecture promotes more effective physical engagement between CAR T cells and tumor cells. We next asked whether this improved engagement translated into stronger CAR T cell activation. Adaptor 4 induced greater phosphorylation of ZAP70 and ERK, and increased CAR T cell degranulation, measured by CD107a expression (**Figure 5d-f**). Together, these data demonstrate that Adaptor 4 improves the strength and persistence of CAR T cell-tumor cell engagement, leading to enhanced proximal CAR signaling and effector activation.

We used Xenium-based transcriptomics to compare CAR T cell distribution and functional states in tumors treated with CD19-CAR T cells combined with either Adaptor 3 or Adaptor 4 (**Figure 5g**). In tumors treated with CD19-CAR T cells and Adaptor 3, CAR T cells were predominantly located at the tumor periphery, where neighboring tumor cells expressed high levels of the T cell recruiting chemokines CXCL9, CXCL10 and CXCL11. These peripheral CAR T cells showed relatively low expression of CCL5 and CXCR6, consistent with an active but spatially restricted recruitment response. In contrast, CD19-CAR T cells combined with Adaptor 4 showed broader intratumoral distribution, accompanied by increased CCL5 and CXCL6 expression. These intratumoral CAR T cells also displayed greater functional heterogeneity, including distinct GZMA- and GZMB-expressing populations, whereas CAR T cells in the Adaptor 3 group predominantly showed GZMB expression at the tumor margin. CXCL9, CXCL10 and CXCL11 expression was less prominent in the Adaptor 4-group at this time point, suggesting a transition from a peripheral recruitment-dominated response to a more established intratumoral CAR T cell response. Together, these findings demonstrate that compared with Adaptor 3, Adaptor 4 promotes deeper CD19 CAR T cell infiltration and is associated with more heterogeneous intratumoral CAR T cell states. We therefore further investigated how CAR T cell state varied with their spatial position within the tumor.

Adaptor 4 promotes spatial differentiation of intratumoral CAR T cells

To further characterize CAR T cell phenotypes within Adaptor 4-treated tumors, cells were grouped according to their spatial distribution in regions defined as “tumor core, inner, edge or outside the tumor” (**Figure 6a**). Module analysis revealed a clear spatial transition, with peripheral CAR T cells showing features associated with a less differentiated, memory-like phenotype, whereas the deeply infiltrating CAR T cells were enriched for cytotoxic and activation programs (**Figure 6b**). Consistent with this, peripheral cells expressed higher levels of TCF7, IL7R, CCR7, SELL, CD27 and CD28, while inner and core CAR T cells expressed higher levels of GZMB, GNLY, NKG7, and PRF1, together with effector-associated transcriptional factors and checkpoint molecules (**Figure 6c**). This spatial organization suggests that CAR T cells within the tumor interior displayed features of a more activated cytotoxic state. Conversely, peripheral CAR T cells retained a less differentiated phenotype that may provide a reservoir for continued responses. Such spatial differentiation was not evident with Adaptor 3, where CAR T cells remained largely confined to the tumor margin, and showed a more uniformly activated/effector-associated phenotype, with no correlation

observed between their phenotypes and their intratumoral localization (**Supplementary Figures 7**). Overall, Adaptor 4 induced a better functional state of CD19-CAR T cells relative to Adaptor 3 *in vivo*, supported by enhanced effector, memory, activation, signaling and trafficking signatures, while maintaining lower levels of exhaustion markers (**Supplementary Figures 8**).

Given these spatial differences in CAR T cell state, we next examined whether deeper CAR T cell infiltration was associated with TME remodeling. Compared with tumor cells at the edge, those within the inner and core regions showed stronger inflammatory and immune response programs, including increased chemokines, IFN-response, stress and antigen-presentation signatures (**Figure 6d**). Consistent with this, spatial analysis of the top differentially expressed genes in non-T cells revealed a distinct core-associated transcriptional profile, including increased FN1, VEGFA, TNF, CDKN1A, S100A9 and IRF5, indicative of local inflammatory, stress and tissue-remodeling responses (**Figure 6e**). These changes were concentrated in regions containing deeply infiltrating CAR T cells and in tumor cells located close to CAR T cells, suggesting that tumor penetration and local CAR T cell activation were associated with a more inflammatory surrounding microenvironment.

Together, these findings show that Adaptor 4 enables CAR T cell penetration and retention within the tumor core, where increased tumor engagement is associated with deeper CAR T cell penetration, spatially distinct CAR T cell states, and localized inflammatory remodeling of the TME. CAR T cells within the tumor interior exhibited a more activated cytotoxic phenotype, while adjacent tumor regions showed enhanced inflammatory and stress-associated programs. In contrast, Adaptor 3 responses remained largely restricted to the tumor periphery, providing a potential explanation for its weaker antitumor activity.

Adaptor 4 is effective with patient-derived CAR T cells and induces durable anti-tumor responses

To assess the clinical relevance of the Adaptor 4 platform, we generated CD19-CAR T cells from three patients with advanced solid tumors previously enrolled in the Lewis Y (LeY) CAR T cell trial (ClinicalTrials.gov: NCT03851146). We first tested CD19-CAR T cells generated from patient LeY019. In combination with Adaptor 4, these cells eradicated established MDA-MB-468-HER2 tumors in all six mice and significantly prolonged survival (**Figure 7a-b**). We

then tested CAR T cells from two additional patients (LeY009 and LeY020) and observed consistent anti-tumor activity across all three donors (**Figure 7c**). Importantly, long-term tumor-free mice retained detectable CD19-CAR T cells in the spleen (**Figure 7d**), demonstrating persistence of the adoptively transferred CAR T cells. Furthermore, these mice successfully rejected a subsequent MDA-MB-468-HER2 tumor rechallenge in the presence of Adaptor 4 (**Figure 7e-f**).

Together, these findings demonstrate that Adaptor 4 can effectively redirect patient-derived CD19-CAR T cells against solid tumors, support long-term CAR T cell persistence and durable anti-tumor protection.

Discussion

In this study, we redesigned and improved a bispecific Adaptor platform, extending the activity of CD19-CAR T cells to HER2-positive solid tumors. Through iterative Adaptor design, we improved protein manufacturability and tumor penetration while maintaining sufficient serum persistence, culminating in a compact nanobody-based Adaptor 4. Compared with previous Adaptors, Adaptor 4 enhanced CD19-CAR T cell-tumor engagement and signaling, promoted deeper intratumoral infiltration and was associated with spatially distinct CAR T cell states, mediating durable antitumor responses across multiple solid tumor models. Importantly, the approach remained effective with CD19-CAR T cells generated from patients with advanced solid cancers. Long-term tumor-free mice retained detectable CAR T cells, while rechallenge experiments demonstrated tumor rejection following Adaptor 4 re-administration.

CAR T cell efficacy in solid tumors is commonly limited by poor tumor infiltration, and the immunosuppressive TME[5]. Our findings suggest that the quality of CAR-target engagement is another important determinant of therapeutic activity. Using CARs with identical backbones in paired tumor contexts, CD19-CAR T cells were shown to consistently outperform HER2-CAR T cells in solid tumor models despite comparable activity in conventional *in vitro* assays and leukemia models. These results were associated with stronger target-cell avidity, proximal signaling, degranulation, and intratumoral infiltration, suggesting that differences in CAR-target engagement that appear modest in conventional assays can become functionally important within the more restrictive environment of solid tumors. Thus, CAR-target interaction and signaling quality should be considered alongside antigen expression and tumor

biology when selecting CARs for solid tumor applications. Moreover, our results support a strong rationale to harness the favorable CD19-CAR T cells for solid tumor treatment.

Several previous studies have indeed established the feasibility of redirecting CD19-CAR T cells toward solid tumors. Aalipour *et al*. used an oncolytic vaccinia virus to deliver murine CD19 to B16 melanoma via intra-tumoral injection, which enabled CD19-CAR T cells to recognize otherwise CD19-negative cancer cells[8]. Park *et al*. demonstrated a similar strategy and showed anti-tumor efficacy in both human xenograft and immunocompetent mouse models[9]. More directly related to our approach, Ambrose *et al*. engineered CD19-CAR T cells to secrete CD19-anti-HER2 bispecific bridging proteins[10], whereas Hombach *et al*. co-administered CD19-CAR T cells with purified CD19-anti-HER2 recombinant proteins[11]. Both approaches were evaluated in SKOV3 ($HER2^+$) human xenograft models. Although Ambrose *et al*. demonstrated anti-tumor efficacy *in vivo*, constitutive secretion requires additional CAR T cell engineering. In addition, uncontrolled ubiquitous secretion of CD19-anti-HER2 proteins poses higher risks of on-target, off-tumor toxicity and early T cell exhaustion from over-activation, warranting additional regulatory mechanisms that enforce localized gene expression for risk mitigation[19,20]. Although Hombach *et al*. avoided additional CAR engineering, this studyreported only modest *in vivo* anti-tumor activity. Furthermore, the pharmacokinetics and dosing of the engagers were not examined. Our early Adaptor 1 and 2 formats, which were structurally similar to Hombach *et al*.'s CD19-anti-ErbB2 engager, revealed limitations in protein production and in vivo persistence, respectively. Limited *in vivo* persistence of Adaptor 2 resulted in poor treatment efficacy in an MDA-MB-468-HER2 xenograft model, despite effective CD19-CAR redirection *in vitro.* The incorporation of an Fc domain into Adaptor 3 significantly extended systemic persistence and improved therapeutic activity, although remained limited by poor tumor penetration. Nonetheless, these prior studies and our early Adaptor development work provided an important proof-of-concept that CD19-CAR T cells can be extended beyond CD19-expressing malignancies, while highlighting the need for an improved Adaptor design capable of achieving more sustained anti-tumor activity in solid tumors.

Drawing from the insights above, our novel Adaptor 4 design introduced several improvements over Adaptors 1-3 and previously published designs. Adaptor 4 incorporated a more compact, monomeric VHH-based design that retained sufficient serum persistence via albumin binding

while increasing potency. Indeed, Adaptor 4 mediated stronger CAR T cell-tumor cell engagement, enhanced proximal signaling and degranulation, and promoted deeper CAR T cell infiltration. Lattice light-sheet imaging further suggested that multivalent engagement enabled by Adaptor 4 may permit repeated or simultaneous cytotoxic interactions with individual tumor cells, potentially increasing cumulative tumor cell killing[21]. Spatial profiling further revealed distinct CAR T cell states according to intratumoral location, together with localized inflammatory remodeling of the TME. Thus, the improved efficacy of Adaptor 4 appears to arise from balancing systemic persistence with efficient tumor penetration and effective CAR-target engagement. By addressing the limitations identified with our earlier Adaptors, Adaptor 4 achieved complete tumor regression and durable antitumor responses in established solid tumor models. Together, these findings represent a significant therapeutic and mechanistic advance in CD19-CAR T cell redirection for solid tumor treatment.

Although we recognize the use of human xenografts in immunodeficient mice does not fully recapitulate the complexity of human solid tumor settings, a central aim of this study was to evaluate the Adaptor platform in conjunction with clinically validated FMC63-based CD19-CARs. The FMC63 scFv used here is the targeting domain employed in four FDA-approved CD19 CAR T-cell products[22]. Testing this same human CAR-antigen interaction in an immunocompetent murine system is not readily feasible without introducing a surrogate CAR-antigen pair. Further development of murine Adaptor reagents and murine CARs will enable evaluation of this strategy in immunocompetent tumor models and provide additional insight into its activity within an intact immune microenvironment.

In summary, our findings identify CAR-antigen interactions as an important determinant of CAR T cell performance in solid tumors and demonstrate that favorable properties of CD19-CAR T cells can be used through an extracellular Adaptor strategy. The compact Adaptor 4 format enables effective tumor engagement, deeper infiltration and is associated with spatially distinct CAR T cell states. This approach remained effective with patient-derived CAR T cells and generated durable anti-tumor protection, including protein against tumor rechallenge following Adaptor 4 re-administration. These findings establish a framework for extending the potency of clinically proven CD19-CAR T cells to solid tumors.

Material and methods

CAR Constructs

The CD19-CAR construct adopting an FMC63 scFv (GenBank: ADM64594.1) and HER2-CAR construct adopting an FRP5 scFv[23] were designed in house and synthesized by Genscript. The CAR plasmid and lentiviral packaging plasmids including pMDLg/pRRE, pRSV-Rev and pMD2.G (Addgene) were used to transfect HEK 293T cells with Lipofectamine 3000 (Thermo Fisher) to produce lentiviral vectors.

Generation of human CAR T cells

Human PBMCs from healthy donors were provided by Australian Red Cross Blood Service and isolated as described previously[24]. Frozen apheresis products were obtained from three individual patients enrolled in the CAR-T cell clinical trial (NCT03851146) under the project HREC 16/17. To activate T cells, PBMCs were cultured in 1:100 T cell TransAct (Miltenyi Biotec) in TexMACS medium (Miltenyi Biotec) containing recombinant human IL7 and IL15 (Miltenyi Biotec) 12.5 ng/mL. 48 hours post activation, T cells were transduced with CAR lentiviral vectors and maintained in TexMACS medium containing IL7 and IL15 and used between 5-13 days post transduction as described previously[25].

Human cell lines

NALM6 and SKOV3 cell lines were cultured in complete RPMI-1640 (Gibco), whereas MDA-MB-468 and MDA-MB-231 cell lines were cultured in complete DMEM (Gibco), supplemented with 10% FBS, 2 mM GlutaMAX (Gibco), 10 mM HEPES (Gibco), 2 mM MEM Non-Essential Amino Acids (Gibco), 1 mM Sodium Pyruvate and 100 U/mL Penicillin-streptomycin and cultured at 37°C. All cell lines were regularly tested to ensure they were *Mycoplasma* negative.

CD19 gene was knocked out of NALM6 cells using the CRISPR-Cas9 system. Three single guide RNA sequences targeting CD19 (CTAGGTCCGAAACATTCCAC, AGAGCTGAAGGACGATCGCC and CGAGGAACCTCTAGTGGTGA) synthesized by Synthego were used to form Cas9/sgRNA ribonucleoprotein complexes with the Cas9 Protein and delivered to NALM6 cells via electroporation on a 4D-Nucleofector X unit (Lonza). $CD19^-$ NALM6 cell clones were selected by fluorescence-activated cell sorting (FACS).

NALM6 (CD19KO or parental), MDA-MB-468, MDA-MB-231 or SKOV3 cells were transduced with lentiviral vectors expressing the full length human CD19 or HER2 gene, firefly luciferase (eFFly) and mCherry under the EF1α promoter and positive populations were selected by FACS.

Mouse models

NSG mice were bred on-site in the Animal Facility at Peter MacCallum Cancer Centre (Peter Mac). In leukemia xenograft models, NSG mice were injected with 5×10^5 luciferase/mCherry-expressing NALM6 cells ($CD19^+$ or $HER2^+$) in 200 μL PBS intravenously via the tail vein. Leukemia burden was assessed using IVIS (Perkin Elmer) until the ethical experiment endpoint. Briefly, animals were anesthetized and intraperitoneally injected with VivoGlo Luciferin (Promega) at 150 mg/kg. Bioluminescence was measured and total flux (p/s) per mouse was quantified in regions of interest (ROI). In solid tumor xenograft models, 1×10^6 NALM6 cells ($CD19^+$ or $HER2^+$) in 20 μL Matrigel (Corning): PBS = 1:1 volume ratio or 1×10^6 MDA-MB-468 cells or MDA-MB-231-HER2 cells ($CD19^+$ or $HER2^+$) in 20 μL PBS were injected into the left 4^{th} quadrant mammary glands of NSG mice; 2×10^6 SKOV3 cells ($CD19^+$ or $HER2^+$) in 100 μL PBS were injected subcutaneously to the right flanks of NSG mice. Mice were treated once tumors grew larger than 25 mm^2. Tumor areas were measured and calculated as length × width. In survival studies, tumor sizes above 100 mm^2 was used as the experiment endpoint. All mice received 0.5 Gy total body irradiation prior to CAR T cell injection on the same day. CD19- and HER2-CAR T cells used in parallel experiments were generated from the same donor PBMC for direct comparison.

In studies evaluating CD19-anti-HER2 Adaptors, NSG mice bearing established MDA-MB-468-HER2 or MDA-MB-231-HER2 tumors received CAR T cells, Adaptors, or the combination treatment. When comparing different Adaptors, doses were adjusted according to molecular weight using 100 μg Adaptor 3 as the reference (Adaptor 2, 36 μg; Adaptor 3, 100 μg; Adaptor 4, 34 μg) to achieve equivalent molar dosing across constructs. In the MDA-MB-468-HER2 model, treatments were administered on days 0, 7 and 14, whereas mice in the MDA-MB-231-HER2 model were treated on days 0, 5 and 10. For combination groups, CAR T cells and Adaptors were co-administered intravenously. For immunohistochemistry and Xenium studies, tumors and spleens were collected at the indicated experimental endpoints, formalin-fixed and paraffin-embedded prior to analysis. For Adaptor 3 studies, tissues were

collected 5 days following treatment. For studies comparing Adaptor 3 and Adaptor 4, tissues were collected 10 days following treatment, corresponding to the time point at which treatment responses diverged between groups. For immunofluorescence studies, tumors were collected 4 days following treatment, embedded in OCT compound and snap frozen prior to sectioning. Unless otherwise indicated, doses used in individual experiments are provided in the corresponding figure legends.

All murine experiments were performed in accordance with the Peter MacCallum Cancer Centre (PMCC) Animal Experimentation Ethics Committee.

Cytokine production assay

CAR T cells were seeded in complete RPMI in a 96-well plate with target cells or plate-bound antibodies including 1 μg anti-CD3 (BioLegend) or 1 μg anti-FLAG (BioLegend). Where applicable, soluble CD19-ECD-anti-HER2 Adaptor protein was added without preincubation with effector or target cells. IFNγ levels in supernatant after overnight incubation were analyzed using the human IFNγ AlphaLISA kit according to manufacturer's protocol (Revvity). Plates were read on Agilent BioTek Cytation 5 with an Alpha filter cube.

Cytotoxicity assays

Luciferase-expressing target tumor cells were co-incubated with CAR T cells in complete RPMI in a white 96-well microplate (Revvity). Target cells alone and target cells in 5% SDS were used as controls. After overnight incubation, 300 μg/mL VivoGlo Luciferin (Promega) was added, and luminescent readings were measured using the Agilent BioTek Cytation 3. Specific luciferase reduction was calculated as: (target cell alone luminescence − sample luminescence)/(target cell alone luminescence − target cell in 5% SDS luminescence) × 100%.

^{51}Cr labelled target tumor cells were co-incubated with CAR T cells in complete RPMI in a 96-well tissue culture plate. Where applicable, 2 mM EGTA was added to samples. Target cell alone and target cell in 5% SDS controls were set up as spontaneous release and total release controls, respectively. After 4-hour incubation, ^{51}Cr release into the supernatant was measured using the Perkin Elmer TriCarb 2910TR scintillation counter. Specific ^{51}Cr release was calculated as (CPM sample − CPM spontaneous release)/(CPM total release − CPM spontaneous release) × 100%.

RNA-Seq

Tumors were enzymatically digested at 37 °C for 20 min rotating at 220 rpm, with 1 mg/mL Collagenase IV (Worthington), 100 µg/mL Hyaluronidase and 75 µg/mL DNase I (Sigma) in RPMI-1640 medium before mechanical dissociation through a 70 µm cell strainer. Spleens were mechanically dissociated through a 70 µm cell strainer before red blood cell lysis. Dissociated cells were sorted by FACS for GFP^+ CAR T cells and $mCherry^+$ tumor cells. RNA was extracted using the miRNeasy kit (Qiagen) according to manufacturer's protocol and purified with AMPure beads (Beckman Coulter). The total RNA quantity was measured using a Qubit RNA HS assay (Thermo Fisher Scientific). 500 ng of total RNA was used for library preparation according to standard protocols (QuantSeq 3'mRNA-seq FWD, Lexogen). Indexed libraries were pooled and sequenced on a NextSeq500 (Illumina). A total of 5–15 million single-end 75 bp reads were generated per sample. Sequence reads were trimmed and aligned to hg38 genome using Cutadapt and HISAT2 packages. Gene counts were obtained from featureCounts. Expression normalization and filtration were performed using Limma. All analysis packages were operated within the Galaxy suite environment (version 24.1). Gene set enrichment analysis (GSEA_v4.3.3) was used for functional enrichment analysis of annotated terms from GO, KEGG and Reactome using the human genome (GRCh38) as background. Statistical analyses for the RNA sequencing were carried out using R version 4.4.1. Packages used for RNA sequencing analysis included limma_3.60.4, GSEA_v4.3.3 and Galaxy suite environment (version 24.1, including Cutadapt, HISAT2, featureCounts and Limma). Packages used for plotting included tidyverse_2.0.0, ComplexHeatmap_2.20.0, EnhancedVolcano_1.22.0 and ggpubr_0.6.0.99.

Lattice light-sheet microscopy

Live CAR T cells were first labelled with anti-CD45-AF647 antibody (Biolegend, clone HI30), then stained with Fluo-4 AM (Thermo Fisher Scientific) according to the manufacturer's instructions to monitor intracellular calcium signaling. NALM6 ($CD19^+$ or $HER2^+$) tumor cells or MDA-MB-468-HER2 tumor cells preincubated with 100 nM Adaptor 3 or Adaptor 4 were stained with SPY555-FastAct (1:500; Cytoskeleton) for 2 h at 37 °C to visualize filamentous actin (F-actin). CAR T cells and tumor cells were combined and imaged using a Lattice light-sheet microscope (Carl Zeiss AG, Oberkochen, Germany). Fluorescence was excited using 488-, 561- and 640-nm lasers. Emission signals were separated using a 640-nm long-pass

dichroic mirror and detected using 495–550-nm and 570–620-nm bandpass filters for Fluo-4 and SPY555-FastAct, respectively, while CD45-AF647 fluorescence was collected in the far-red channel. Time-lapse three-dimensional fluorescence images were acquired. Raw data were de-skewed and deconvoluted using manufacturer's inbuilt lattice light-sheet modules before processed images were further analyzed using Imaris software (v10.1; Oxford Instruments, Abingdon, UK).

Processed data from one representative experiment of three independent experiments were analyzed to compare CD19- and HER2-CAR T cell synapse formation with NALM6 target cells. Potential CAR T cell-tumor cell interactions were defined as pairs in close proximity (estimated surface gap ≤8 μm and centroid distance ≤40 μm). Frames with ROI boundary warnings, CAR T cell or tumor volumes >1000 μm^3, or overlap volumes exceeding 20% of the smaller segmented object were excluded. For pairs that established contact, the largest contact area observed was normalized to CAR T cell size (volume^(2/3)) to generate a size-adjusted peak contact value and the longest consecutive contact time were measured.

Processed data from one representative experiment of three independent experiments were analyzed to compare Adaptor 3 and Adaptor 4 mediated synapse formation between CD19-CAR T cells and MDA-MB-468-HER2 tumor cells. The total number of potential CAR T cell-tumor cell interactions were quantified over the same period for both conditions.

Immunohistochemistry

Tumor and spleen tissues were fixed in 10% neutral buffered formalin and paraffin embedded. Tumor sections (4 μm) were deparaffinized, antigen was retrieved in Tris/EDTA (pH = 9) and endogenous peroxidase activity was blocked using 3% H_2O_2. The sections were then blocked with 5% normal goat serum and incubated with primary anti-CD3 (Abcam, clone SP7) or anti-CD31 antibodies (Abcam, clone EPR17259) for 1 hour at room temperature followed by biotin-linked secondary antibodies (immPRESS, Vector Laboratories) incubated for 1 hour at room temperature. Chromogenic color was developed using 3,3-diaminobenzidine (DAB, Vector Laboratories). Slides were then counter-stained in hematoxylin and coverslips were mounted. Microscopic images were taken using the Olympus BX53 microscope.

Immunofluorescence

Tumor sections (4 μm) from frozen tumor tissues were fixed in 4% paraformaldehyde (PFA) for 10-15 minutes at room temperature and blocked in PBS-/- containing 1% BSA and 10% goat serum for 1 hour. Sections were then stained with primary anti-CD19 antibody (Abcam, clone EPR5906) in PBS-/- containing 1% BSA and 10% goat serum overnight at 4°C. Sections were stained with secondary goat anti-rabbit antibody (Invitrogen) for 1 hour at room temperature. The slides were stained with DAPI (10 μg/mL in PBS-/-). ProLong Glass Antifade Mountant (Invitrogen) was applied to each section and a coverslip was mounted. Microscopic images were taken using the Olympus FV3000 microscope.

Flow cytometry

Surface staining of *in vitro* cell cultures was performed by incubating cells with antibodies in 50 μL FACS buffer ($PBS^{-/-}$ containing 2% FBS, 2 mM EDTA and 0.1% sodium azide) for 20-30 min in the dark at 4ºC. Antibodies for CAR T cell surface staining include anti-FLAG (BioLegend, clone L5), anti-CD3 (BioLegend, clone SK7), anti-CD4 (BD, clone SK3), anti-CD8 (BD, clone RPA-T8), anti-CD45RA (BioLegend, clone HI100), anti-CD62L (BioLegend, clone DREG-56), anti-LAG3 (BioLegend, clone 11C3C65), anti-PD1 (BioLegend, clone EH12.2H7) and anti-TIM3 (BioLegend, clone F38-2E2).

Surface staining of *in vivo* cell suspensions was performed by incubating known fractions of sample with antibodies in 100 μL FACS buffer for 30 min in the dark at 4ºC. CountBright Plus Absolute Counting Beads (Thermo Fisher) were used according to the manufacturer's protocol to determine absolute cell counts.

In CD19-ECD-anti-HER2 Adaptor binding assays, tumor or CAR T cells were incubated with Adaptor protein at indicated concentrations for 30 min at 4ºC, followed by secondary staining for 30 min in the dark at 4ºC.

To quantify surface antigen levels on cancer cells, anti-CD19 (BioLegend, clone HIB19), anti-HER2 (BioLegend, clone 24D2) and Quantum Simply Cellular (Bang Laboratories) were used according to the manufacturer's protocol. To quantify surface CAR levels on CAR T cells, anti-FLAG (BioLegend, clone L5) and QuantiBRITE (BD Biosciences) were used according to the manufacturer's protocol.

To assess intracellular signaling, CD19- or HER2- CAR T cells were incubated with NALM6-CD19 or NALM6-HER2, respectively, at 1:1 ratio in RPMI containing 0.1% FBS for 30 min in a 37ºC water bath. At the end of incubation, samples were immediately fixed in 1:1 volume of BD Cytofix for 10 min at room temperature, washed in PBS, followed by permeabilization in methanol for 10 min on ice. Samples were stained with anti-Zap70 (Y319)/Syk (Y352) (BD, 17A/P-ZAP70) or anti-ERK1/2 (T202/Y204) (BioLegend, clone 6B8B69). Cells were stained with 50 µL buffer ($PBS^{-/-}$ containing 1% FBS and 0.09% sodium azide) for 1 hour in the dark at 4ºC.

To assess degranulation, CD19- or HER2- CAR T cells were incubated with NALM6-CD19 or NALM6-HER2, respectively, at 1:1 ratio in complete RPMI containing anti-CD107a (BioLegend, clone H4A3). After a 2-hour incubation at 37ºC, surface CD107a expression on samples were assessed.

Adaptor production

Adaptor plasmids were designed in house (Adaptors 1-3) or by Aleta Biotherapeutics (Adaptor 4). All constructs were subsequently codon-optimized, synthesized, expressed in CHO cells, and the secreted recombinant proteins were purified by Genscript.

Avidity measurements

Avidity between cancer cells and CAR T cells was measured using a z-Movi Cell Avidity Analyzer (LUMICKS). Cancer cells were seeded in the z-Movi microfluidic chip pre-coated with 0.002% Poly-L-Lysine (PLL) and incubated at 37ºC for 2 hours to form a monolayer with an approximately 95% surface coverage. Seeding densities of NALM6 and MDA-MB-468 cell lines were 180 $\times 10^6$ cells/mL and 100 $\times$ 10^6 cell/mL, respectively. CAR T cells were stained with the CellTrace Far Red Dye (C34564, Thermo Fisher) according to the manufacturer's protocol. Stained CAR T cells (10 $\times$ 10^6 cells/mL, 10 µL) were then introduced into the z-Movi chip and incubated with cancer cell monolayer for 5 min, followed by the application of an acoustic force ramp (0 - 1000 pN) for another 2.5 min. The percentage of CAR T cells (300 - 500 individual cells) detached from the monolayer was calculated using the z-Movi software (Ocean v1.4.1, LUMICKS).

ELISA

To determine the concentration of Adaptors, ELISA plates were coated with anti-FLAG antibody (BioLegend, clone L5) at 1 μg/mL in PBS for testing Adaptors 2 and 3, or with anti-VHH antibody (Genscript) at 1 μg/mL in PBS for testing Adaptor 4, and incubated overnight at 4°C. After washing three times with PBS containing 0.05% Tween-20 (PBST), plates were blocked with 5% skim milk in PBST for 1 hour at room temperature and washed again. Adaptor standards and samples were prepared in blocking buffer and added at 50 μL per well, followed by incubation at room temperature for 2 hours. Plates were washed seven times with PBST and then incubated with biotinylated HER2-HIS (Sino Biological) at 0.5 μg/mL in blocking buffer for detecting Adaptors 2 and 3, or with biotinylated anti-CD19 antibody (Biolenged, clone HIB19) at 1 μg/mL in blocking buffer, for 1 hour at room temperature. Following additional washes, streptavidin-HRP (Cytiva) diluted 1:500 in blocking buffer was added for 30 min in the dark. TMB substrate solution (BD OptEIA) was added at 100 μL per well, and plates were incubated for 30 min at room temperature, protected from light. Reactions were stopped using 1 M H_2SO_4, and absorbance was read at 450 nm using Agilent BioTek Cytation 3.

Xenium-based spatial transcriptomics

Formalin-fixed paraffin-embedded tumor and spleen sections (4 μm) were cut using a Thermo Scientific microtome and mounted onto two Xenium slides following the demonstrated protocol (CG000578). Slides were deparaffinized and de-crosslinked (CG000580), then processed using the 10x Genomics Xenium Human Immuno-Oncology Profiling Panel (380 genes). Probe hybridization, ligation, amplification, and cell segmentation staining were performed according to the Xenium In Situ Gene Expression User Guide (CG000749). The Xenium Analyzer run and onboard analysis (v3.3.0.1) were performed per the Xenium Analyzer User Guide (CG000584), generating transcript coordinates, cell boundaries, and feature-cell matrices. Raw outputs were filtered using Seurat (v5.2.0), retaining transcripts with signal above negative control probes and cells with ≥120 detected genes. T cells were annotated based on canonical markers (CD3D, CD3E, CD4, CD8A, CD8B, FOXP3, IL2RA). Differential expression was assessed using DESeq2 (v1.44.0) in a pseudobulk framework, controlling for library size and batch. Spatial proximity analysis was used to identify cells adjacent to CAR-T cells, and cell-cell communication was inferred using CellChat (v2.2.0).

Statistical analysis

Statistical analyses were performed using GraphPad Prism version 10.2.3 for macOS (GraphPad Software, Boston, Massachusetts USA, www.graphpad.com). Exact statistical tests are indicated in the corresponding figure legends. *P* values (*$P < 0.05$; **$P < 0.01$; ***$P < 0.001$; ****$P < 0.0001$; *ns*, not significant).

Data availability statement

The authors declare that data supporting the findings of this study are available within the article and its supplementary information fields. All other relevant data are available from the corresponding author upon reasonable request.

Acknowledgements

This work was supported by grants from the National Health and Medical Research Council (NHMRC), the National Breast Cancer Foundation (NBCF) of Australia, mRNA Victoria Research Programs, the Australian Government Department of Education, the CASS Foundation, and the University of Sydney Collaborative Research Equipment Grants.

CYS, PKD and JAT were supported by NHMRC Investigator Grants and a Victorian Cancer Agency Mid-Career Fellowship. YB received support from a Cancer Council Victoria Postdoctoral Fellowship, LAJ is a Snow Medical Research Foundation Fellow. RX was supported by a Peter Mac Foundation PhD Scholarship and an AusHealth CureCell Award, RH by a Li Ka Shing Foundation Clinical Research Training Program, EGP by a Research Training Program (RTP) PhD Scholarship and an AusHealth CureCell Award, and HJW by RTP and Tour de Cure PhD Scholarships.

We thank the Peter MacCallum Cancer Research Flow Core (RRID:SCR_025550), Centre for Advanced Histology and Microscopy (RRID:SCR_025432), Victorian Centre for Functional Genomics (RRID:SCR_025582), Molecular Genomics Core (RRID:SCR_025695), Research Laboratory Support Services (RRID:SCR_025699) and Cancer Research Animal Core for their respective contributions to this study. The authors acknowledge the use of ChatGPT for editorial support in improving the clarity and readability of the manuscript.

Author contributions

Conception and design: R.X., M.H.K, P.K.D and C.Y.S.

Experimental work: R.X., Y.B, Y.W, B.v.S, X.Z, R.H, D.Z, O.H, E.G.P, B.J.L, J.J, H.J.W, C. D and C.Y.S.

Data analysis and interpretation: All the authors.

Write and editing: All the authors.

Supervision: M.D, L.A.J, M.H.K, P.K.D and C.Y.S.

Competing interests

C.S, B.v.S and M.H.K are scientific founders of Currus Biologics. P.R is the CSO and C.A is a PI of Aleta Bio.

References

1 Bouchkouj, N., Przepiorka, D. & Fashoyin-Aje, L. A. Obecabtagene Autoleucel for B-Cell Acute Lymphoblastic Leukemia. *JAMA* **333**, 1354-1355 (2025). https://doi.org/10.1001/jama.2024.28312

2 Chan, J. D. *et al.* Cellular networks controlling T cell persistence in adoptive cell therapy. *Nat Rev Immunol* **21**, 769-784 (2021). https://doi.org/10.1038/s41577-021-00539-6

3 Sterner, R. C. & Sterner, R. M. CAR-T cell therapy: current limitations and potential strategies. *Blood Cancer J* **11**, 69 (2021). https://doi.org/10.1038/s41408-021-00459-7

4 Slaney, C. Y., Kershaw, M. H. & Darcy, P. K. Trafficking of T cells into tumors. *Cancer Res* **74**, 7168-7174 (2014). https://doi.org/10.1158/0008-5472.CAN-14-2458

5 Albarran-Fernandez, V. *et al.* Unlocking the potential of engineered immune cell therapy for solid tumors. *Nat Commun* **16**, 1144 (2025). https://doi.org/10.1038/s41467-025-56527-0

6 Larson, R. C. *et al.* CAR T cell killing requires the IFNgammaR pathway in solid but not liquid tumours. *Nature* **604**, 563-570 (2022). https://doi.org/10.1038/s41586-022-04585-5

7 Long, A. H. *et al.* 4-1BB costimulation ameliorates T cell exhaustion induced by tonic signaling of chimeric antigen receptors. *Nat Med* **21**, 581-590 (2015). https://doi.org/10.1038/nm.3838

8 Aalipour, A. *et al.* Viral Delivery of CAR Targets to Solid Tumors Enables Effective Cell Therapy. *Mol Ther Oncolytics* **17**, 232-240 (2020). https://doi.org/10.1016/j.omto.2020.03.018

9 Park, A. K. *et al.* Effective combination immunotherapy using oncolytic viruses to deliver CAR targets to solid tumors. *Sci Transl Med* **12** (2020). https://doi.org/10.1126/scitranslmed.aaz1863

10 Ambrose, C. *et al.* Anti-CD19 CAR T cells potently redirected to kill solid tumor cells. *PLoS One* **16**, e0247701 (2021). https://doi.org/10.1371/journal.pone.0247701

11 Hombach, A. A., Ambrose, C., Lobb, R., Rennert, P. & Abken, H. A CD19-Anti-ErbB2 scFv Engager Protein Enables CD19-Specific CAR T Cells to Eradicate ErbB2+ Solid Cancer. *Cells* **12**, 248 (2023). https://doi.org/10.3390/cells12020248

12 Thakur, A., Scholler, J., Schalk, D. L., June, C. H. & Lum, L. G. Enhanced cytotoxicity against solid tumors by bispecific antibody-armed CD19 CAR T cells: a proof-of-

concept study. *Journal of Cancer Research and Clinical Oncology* **146**, 2007-2016 (2020). https://doi.org/10.1007/s00432-020-03260-4

13 Slaney, C. Y., Wang, P., Darcy, P. K. & Kershaw, M. H. CARs versus BiTEs: A Comparison between T Cell-Redirection Strategies for Cancer Treatment. *Cancer Discov* **8**, 924-934 (2018). https://doi.org/10.1158/2159-8290.CD-18-0297

14 Chen, B.-C. *et al.* Lattice light-sheet microscopy: Imaging molecules to embryos at high spatiotemporal resolution. *Science* **346**, 1257998 (2014). https://doi.org/10.1126/science.1257998

15 Qiu, Y. *et al.* Mechanical force determines chimeric antigen receptor microclustering and signaling. *Mol Ther* **32**, 1016-1032 (2024). https://doi.org/10.1016/j.ymthe.2024.02.006

16 Pyzik, M., Kozicky, L. K., Gandhi, A. K. & Blumberg, R. S. The therapeutic age of the neonatal Fc receptor. *Nature Reviews Immunology* **23**, 415-432 (2023). https://doi.org/10.1038/s41577-022-00821-1

17 Lobner, E. *et al.* Getting CD19 Into Shape: Expression of Natively Folded "Difficult-to- Express" CD19 for Staining and Stimulation of CAR-T Cells. *Front Bioeng Biotechnol* **8**, 49 (2020). https://doi.org/10.3389/fbioe.2020.00049

18 Klesmith, J. R. *et al.* Retargeting CD19 Chimeric Antigen Receptor T Cells via Engineered CD19-Fusion Proteins. *Molecular Pharmaceutics* **16**, 3544-3558 (2019). https://doi.org/10.1021/acs.molpharmaceut.9b00418

19 Zhang, L. *et al.* Improving Adoptive T Cell Therapy by Targeting and Controlling IL-12 Expression to the Tumor Environment. *Molecular Therapy* **19**, 751-759 (2011). https://doi.org/https://doi.org/10.1038/mt.2010.313

20 Chen, A. X. Y. *et al.* Rewiring endogenous genes in CAR T cells for tumour-restricted payload delivery. *Nature* **644**, 241-251 (2025). https://doi.org/10.1038/s41586-025-09212-7

21 Khazen, R. *et al.* Functional heterogeneity of cytotoxic T cells and tumor resistance to cytotoxic hits limit anti-tumor activity in vivo. *The EMBO Journal* **40**, EMBJ2020106658 (2021). https://doi.org/10.15252/embj.2020106658

22 Volta, L. & Gill, S. I. In vivo generation of CAR T cells: biology, delivery platforms, clinical promise, and translational challenges. *Blood Immunology & Cellular Therapy* **2**, 100027 (2026). https://doi.org/https://doi.org/10.1016/j.bict.2025.100027

23 Wels, W., Harwerth, I. M., Mueller, M., Groner, B. & Hynes, N. E. Selective inhibition of tumor cell growth by a recombinant single-chain antibody-toxin specific for the erbB-2 receptor. *Cancer Res* **52**, 6310-6317 (1992).

24 Ali, A. I. *et al.* A Histone Deacetylase Inhibitor, Panobinostat, Enhances Chimeric Antigen Receptor T-cell Antitumor Effect Against Pancreatic Cancer. *Clin Cancer Res* **27**, 6222-6234 (2021). https://doi.org/10.1158/1078-0432.CCR-21-1141

25 Zhang, X. *et al.* Optimised modular anti-FLAG CAR T cells for solid tumor therapy. *Clin Transl Immunology* **14**, e70046 (2025). https://doi.org/10.1002/cti2.70046

Main Figures

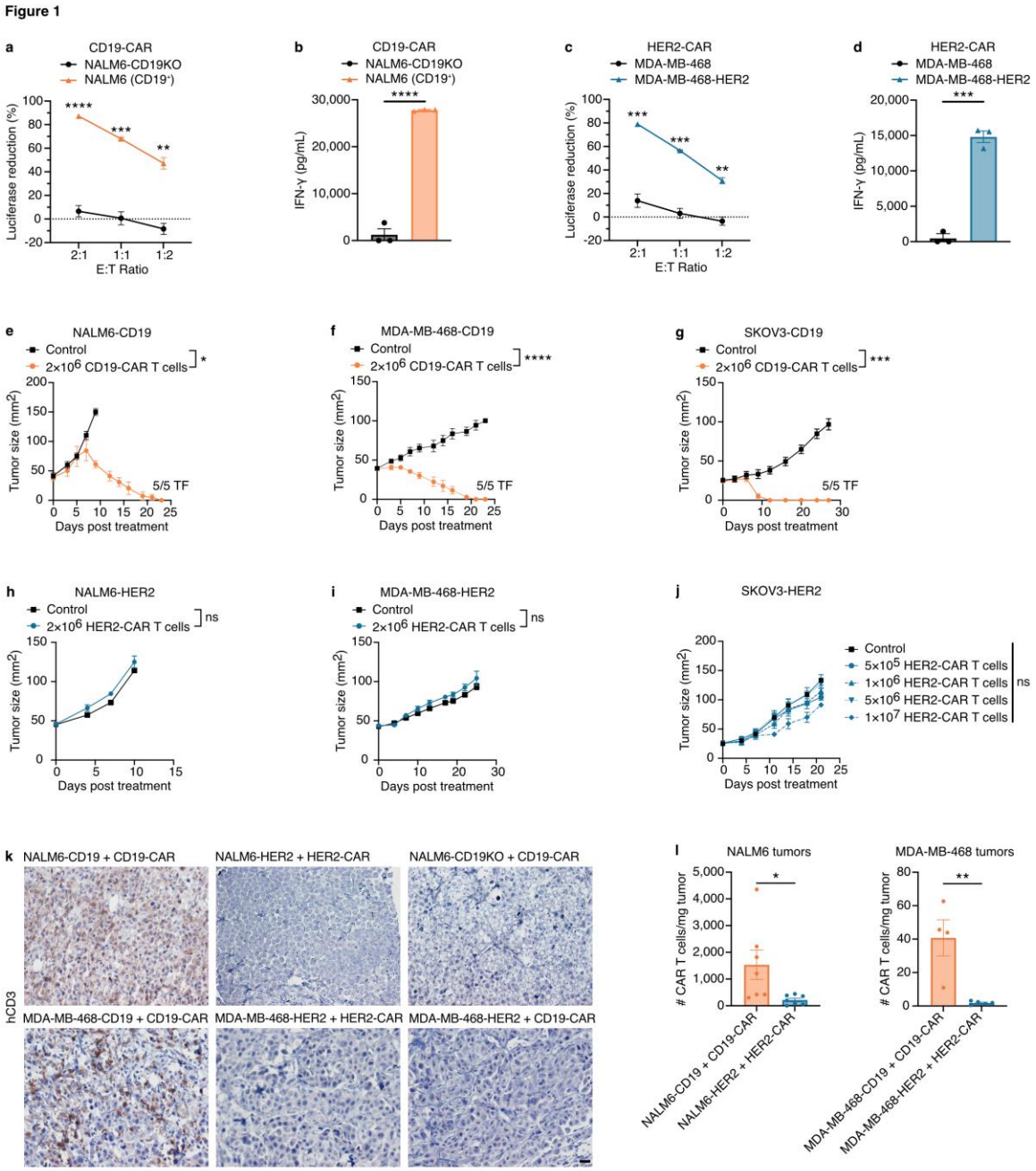


Figure 1. CD19-CAR but not HER2-CAR T cells inhibit solid tumor growth in NSG mice despite similar CAR designs.

a Luciferase reduction of NALM6-CD19KO or NALM6 (CD19$^+$) cells following overnight co-incubation with CD19-CAR T cells at various E:T ratios. E:T ratio, effector to target ratio. **b** IFN-γ production by CD19-CAR T cells following overnight co-incubation with NALM6-CD19KO or NALM6 (CD19$^+$) cells at 1:1 ratio. **c** Luciferase reduction of MDA-MB-468 or MDA-MB-468-HER2 cells following overnight co-incubation with HER2-CAR T cells at various E:T ratios. **d** IFN-γ production by HER2-CAR T cells following overnight incubation

with MDA-MB-468 or MDA-MB-468-HER2 cells at 1:1 ratio. **a-d** Data are mean ± SEM technical triplicates (representative experiment of three independent experiments using different healthy donors). Tumor growth curves of NSG mice bearing **e** NALM6-CD19 mammary gland tumors, **f** MDA-MB-468-CD19 mammary gland tumors, or **g** SKOV3-CD19 subcutaneous tumors receiving no treatment (control) or CD19-CAR T cells. Tumor growth curves of NSG mice bearing **h** NALM6-HER2 mammary gland tumors, **i** MDA-MB-468-HER2 mammary gland tumors or **j** SKOV3-HER2 subcutaneous tumors receiving no treatment (control) or HER2-CAR T cells, (NALM6-HER2, control: n = 4, SKOV3-HER2, all groups: n = 3, all other groups: n = 5). **e-j** Data are mean ± SEM of individual mice. CAR T cells were derived from the same healthy donor in paired models, i.e., in **e** and **h**, **f** and **i**, **g** and **j**. TF, tumor free. **k** Immunohistochemistry (IHC) images showing human CD3 staining in mammary gland xenograft tumors treated with 2×10^6 CD19- or HER2-CAR T cells, 9 days post treatment. Scale bar represents 20 μm. Images are representative of xenografts from three individual mice treated with CAR T cells derived from the same human donor. **l** Numbers of tumor-infiltrating CD19- or HER2-CAR T cells normalized to tumor weight, analyzed by flow cytometry 9 days post treatment. For NALM6 tumors, data are mean ± SEM pooled from two independent experiments involving CAR T cells from two healthy donors (n = 4 and n = 3 mice each, where mice within each experiment received CAR T cells derived from the same donor). For MDA-MB-468 tumors, data are mean ± SEM of individual mice receiving CAR T cells derived from the same healthy donor (n = 4 mice). Significance determined by unpaired Student's *t*-test (two-tailed, **a-i, l**) or one-way ANOVA (Dunnett's multiple comparisons, **j**). *P* values (*$P < 0.05$; **$P < 0.01$; ***$P < 0.001$; ****$P < 0.0001$; *ns*, not significant).

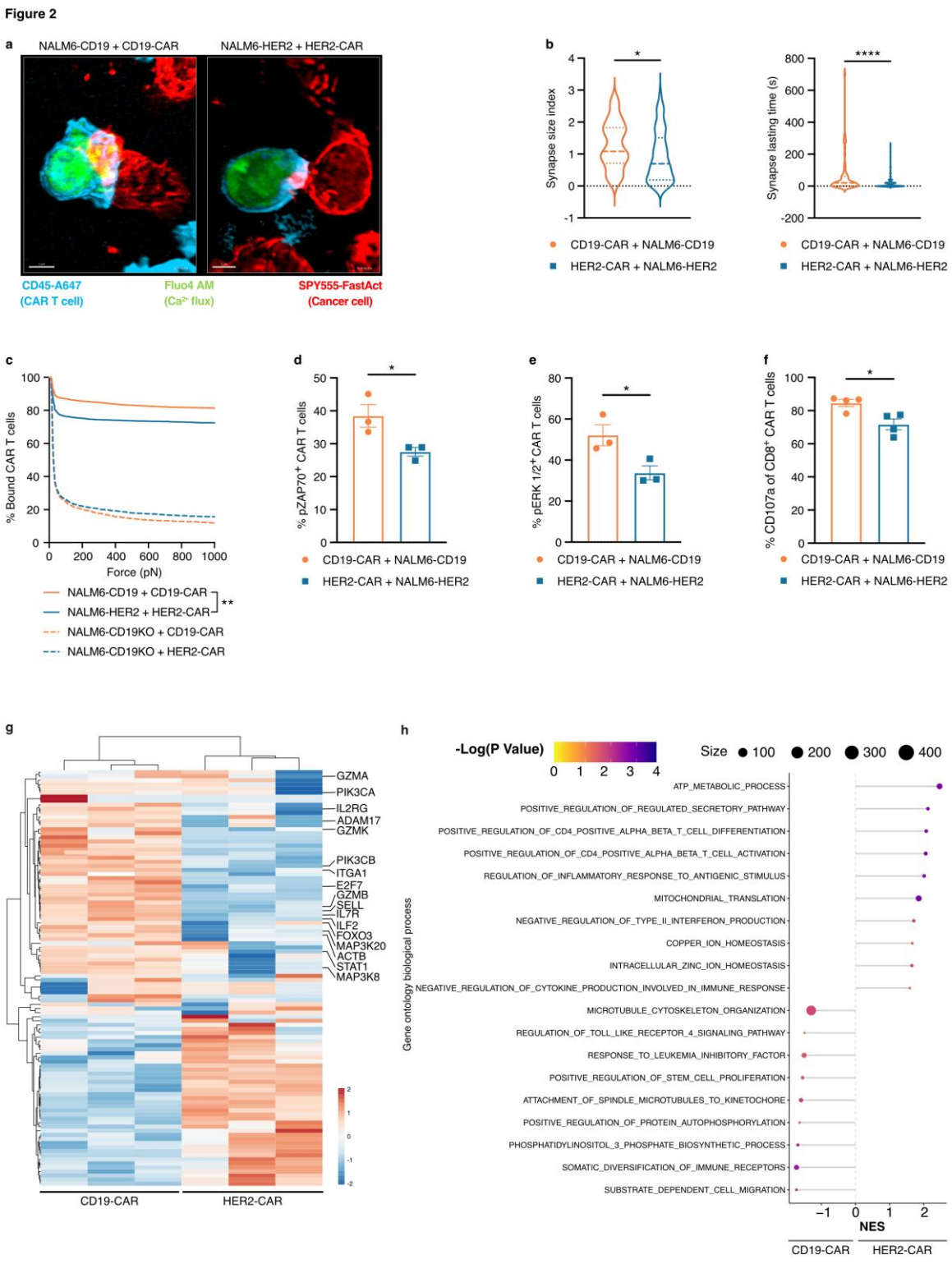


Figure 2. CD19-CAR T cells show better target cell engagement, signaling, activation and cytotoxicity than HER2-CAR T cells.

a Representative image of synapse formation during CD19- (left) or HER2- (right) CAR T cell/tumor cell interactions of three independent experiments involving different healthy

donors. Scale bar represents 2 μm (left) or 3 μm (right). **b** Synapse size index (left) calculated as peak contact area between interacting CD19-CAR T cells and NALM6-CD19 tumor cells or HER2-CAR T cells and NALM6-HER2 tumor cells, normalized to CAR T cell size (volume^(2/3)). Synapse lasting time (right) measured by longest consecutive contact time between CAR T cells and target tumor cells. Data are individual cell-cell interactions from one representative experiment of three independent experiments. Dashed lines represent median values and dotted lines represent quartiles. **c** Percentage of CD19- or HER2-CAR T cells remaining bound to antigen-positive or antigen-negative NALM6 tumor cells after application of indicated acoustic forces, as measured by z-Movi. Data represent mean of pooled values. (NALM6-CD19 + CD19-CAR T cells, n = 4 independent experiments, technical duplicates. Other groups, n = 3 independent experiments, technical duplicates or triplicates.) Percentage of **d** $pZAP70^+$ or **e** pERK $1/2^+$ CAR T cells when co-incubated with antigen-positive tumor cells for 30 min. **f** Percentage of $CD107a^+$ CAR T cells when co-incubated with antigen-positive tumor cells for 2 hours. **d-e** Data are mean ± SEM of three independent experiments involving different healthy donors. **f** Data are pooled mean ± SEM of two independent experiments involving different healthy donors (n = 1 and n = 3 each). **g** Heatmap showing significantly differential immune-related RNA-seq features between CD19- and HER2-CAR T cells isolated from NALM6-CD19 or NALM6-HER2 xenografts, respectively. Data are from n = 4 mice receiving CAR T cells derived from the same donor. mRNA expression is row centered, and unit variance scaled. Genes and samples are ordered by average correlation clustering. **h** Dot plot showing gene set enrichment analysis of Gene Ontology Biological Process (GOBP) terms for CAR T cells in **g**. Dot color represents the false discovery rate (FDR) value for each enriched GO term. Dot size represents the number of genes overlapping the GOBP terms. The GOBP terms with a negative normalized enrichment score (NES) are enriched in CD19-CAR T cells while terms with a positive NES are enriched in HER2-CAR T cells. Significance determined using one-way ANOVA (Sidak's multiple comparisons test, **c**) or unpaired Student's t-test (two-tailed, **d-f**). *P* values (*$P < 0.05$; **$P < 0.01$; ***$P < 0.001$; ****$P < 0.0001$; *ns*, not significant).

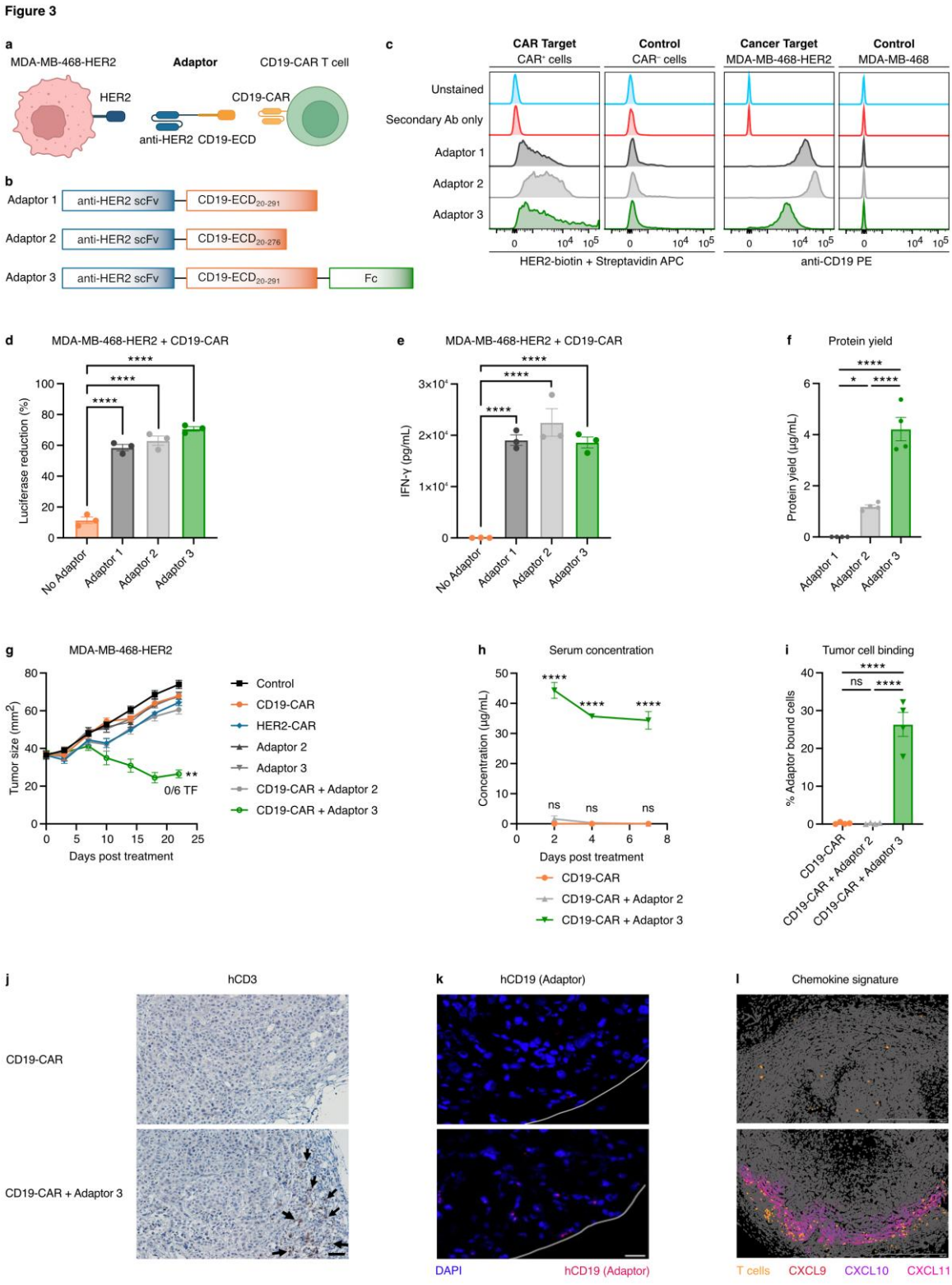


Figure 3. Adaptor proteins redirect CD19-CAR T cell function to MDA-MB-468-HER2 solid tumors.

a Schematic overview of the CD19-anti-HER2 Adaptor approach. **b** Schematic overview of Adaptors designs 1-3. **c** Adaptor binding to CAR^+ or CAR^- cell within the analyzed CD19-

CAR T cell population, detected with biotinylated HER2 protein and streptavidin-APC (left); Adaptor binding to MDA-MB-468-HER2 or MDA-MB-468 cells, detected with anti-CD19 PE (right). **d** Luciferase reduction of MDA-MB-468-HER2 cells following overnight co-incubation with CD19-CAR T cells at 1:1 ratio alone or with 10 nM Adaptor 1 or 2, or 5 nM Adaptor 3. **e** IFN-γ production by CD19-CAR T cells following overnight co-incubation with MDA-MB-468-HER2 at 1:1 ratio alone or with 100 nM Adaptor 1 or 2, or 50 nM Adaptor 3. **f** Protein yield of Adaptor 1, 2 or 3 in HEK293T cell supernatant, 72 hours after plasmid DNA transfection. **d-f** Data are representative of three independent experiments involving different healthy donors, shown as mean ± SEM (technical triplicates). **g** Tumor growth curves of NSG mice bearing MDA-MB-468-HER2 intra-mammary fat pad tumors receiving no treatment, 5 × 10^6 CD19-CAR T cells, 5 × 10^6 HER2-CAR T cells, 36 μg Adaptor 2, 5 × 10^6 CD19-CAR T cells in combination with 36 μg Adaptor 2, 100 μg Adaptor 3 or 5 × 10^6 CD19-CAR T cells in combination with 100 μg Adaptor 3 (n = 5 per group). Data are shown as mean ± SEM of individual mice receiving CAR T cells from the same donor. TF, tumor free. **h** Adaptor concentrations in serum from MDA-MB-468-HER2 tumor bearing NSG mice receiving 5 × 10^6 CD19-CAR T cells alone or with 100 μg Adaptor 2 or 100 μg Adaptor 3, collected at 2-, 4- and 7-days post treatment. (n = 3 per group). Data are shown as mean ± SEM of individual mice receiving CAR T cells from the same donor. **i** Percentage of Adaptor bound MDA-MB-468-HER2 tumor cells detected via FLAG-tag from NSG mice receiving 5 × 10^6 CD19-CAR T cells alone or with 36 μg Adaptor 2 or 100 μg Adaptor 3 at 6 days post treatment (n = 4 per group). Data are shown as mean ± SEM of individual mice receiving CAR T cells from the same donor. **j** Immunohistochemistry images showing human CD3 staining in MDA-MB-468-HER2 mammary gland xenograft tumors treated with 5 × 10^6 CD19-CAR T cells or 5 × 10^6 CD19-CAR T cells in combination with 30 μg Adaptor 3, 5 days post treatment. Images are representative of n = 3 individual mice receiving CAR T cells from the same healthy donor. **k** Immunofluorescence images showing human CD19 staining in MDA-MB-468-HER2 mammary gland xenograft tumors treated with 5 × 10^6 CD19-CAR T cells or 5 × 10^6 CD19-CAR T cells in combination with 100 μg Adaptor 3, 4 days post treatment. Scale bar represents 20 μm. Images are representative of n = 3 individual mice per group receiving CAR T cells from the same healthy donor. **l** Spatial images showing mRNA transcripts in MDA-MB-468-HER2 mammary gland xenograft tumors treated with 5 × 10^6 CD19-CAR T cells or 5 × 10^6 CD19-CAR T cells in combination with 30 μg Adaptor 3, 5 days post treatment. Images are representative of n = 2 individual mice receiving CAR T cells from the same healthy donor.

929 Scale bar represents 500 μm. Significance determined using one-way ANOVA (Sidak's
930 multiple comparisons test, **d-i**). *P* values (**P* < 0.05; ***P* < 0.01; ****P* < 0.001; *****P* <
931 0.0001; *ns*, not significant).
932

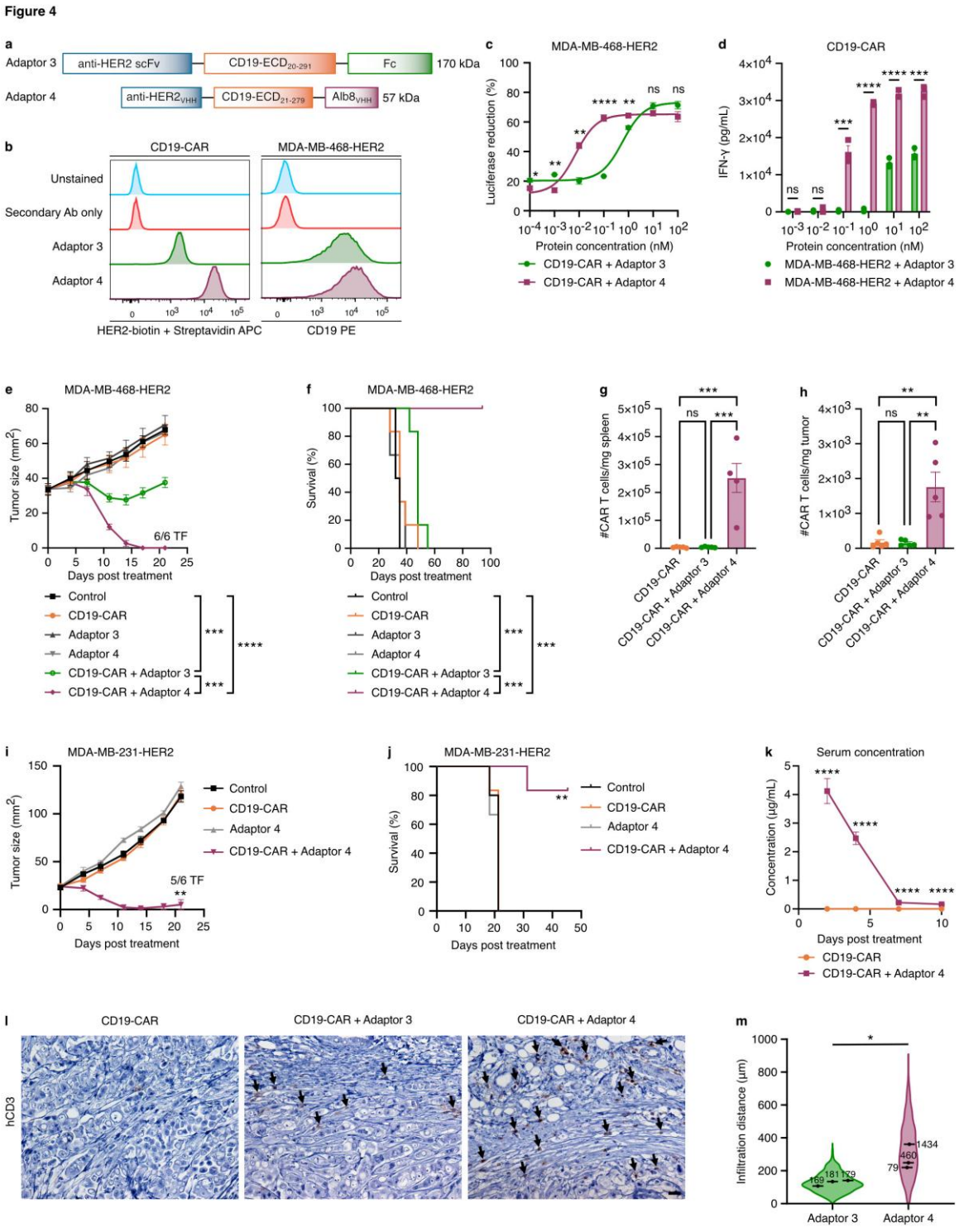


Figure 4. Adaptor 4 redirects CD19-CAR T cells to induce complete tumor clearance and enhanced tumor penetration in an MDA-MB-468-HER2 xenograft model.

a Schematic overview of the Adaptors 3 and 4. **b** Adaptor binding to CD19-CAR T cells, detected with biotinylated HER2 protein and streptavidin-APC (left); Adaptor binding to MDA-MB-468-HER2, detected with anti-CD19 PE (right). **c** Luciferase reduction of MDA-

MB-468-HER2 cells following overnight co-incubation with CD19-CAR T cells at 1:1 ratio with Adaptor 3 or 4 at indicated concentrations. Data are representative of three independent experiments involving different healthy donors, shown as mean ± SEM (technical triplicates). Solid lines represent best-fit nonlinear regression curves, log(inhibitor) vs. response (three parameters) model. EC50 of CD19-CAR + Adaptor 3 = 0.58 nM (95% CI: 0.40–0.85 nM), EC50 of CD19-CAR + Adaptor 4 = 7.2 pM (95% CI: 4.9–10.6 pM). **d** IFN-γ production by CD19-CAR T cells following overnight co-incubation with MDA-MB-468-HER2 at 1:1 ratio with Adaptor 3 or 4 at indicated concentrations. Data are representative of three independent experiments involving different healthy donors, shown as mean ± SEM (technical triplicates). **e** Tumor growth curves of NSG mice bearing MDA-MB-468-HER2 intra-mammary fat pad tumors receiving no treatment (control), 5×10^6 CD19-CAR T cells, 100 μg Adaptor 3, 34 μg Adaptor 4, 5×10^6 CD19-CAR T cells in combination with 100 μg Adaptor 3, or 5×10^6 CD19-CAR T cells in combination with 34 μg Adaptor 4 (n = 6 per group). Data are mean ± SEM of individual mice receiving CAR T cells derived from the same healthy donor. TF, tumor free. **f** Percentage of survival of mice in (**e**). Numbers of **g** spleen-infiltrating or **h** tumor-infiltrating CD19-CAR T cells normalized to organ weight in NSG mice bearing MDA-MB-468-HER2 intra-mammary fat pad tumors, receiving 5×10^6 CD19-CAR T cells, 5×10^6 CD19-CAR T cells in combination with 100 μg Adaptor 3, or 5×10^6 CD19-CAR T cells in combination with 34 μg Adaptor 4 (n = 5 per group), analyzed by flow cytometry 10 days post treatment. Data are mean ± SEM of individual mice receiving CAR T cells derived from the same healthy donor. **i** Tumor growth curves of NSG mice bearing MDA-MB-231-HER2 intra-mammary fat pad tumors receiving no treatment (control), 5×10^6 CD19-CAR T cells, 100 μg Adaptor 4, 5×10^6 CD19-CAR T cells in combination with 100 μg Adaptor 4 (Control, n = 5. All other groups, n = 6). Data are mean ± SEM of individual mice receiving CAR T cells derived from the same healthy donor. **j** Percentage of survival of mice in (**i**). **k** Adaptor concentrations in serum from MDA-MB-468-HER2 tumor bearing NSG mice receiving 5×10^6 CD19-CAR T cells alone or with 100 μg Adaptor 4, collected at 2-, 4-, 7- and 10-days post treatment. (n = 3 per group). Data are mean ± SEM of individual mice receiving CAR T cells derived from the same healthy donor. **l** IHC images of MDA-MB-468-HER2 xenograft tumors, from mice receiving 5×10^6 CD19-CAR T cells, 5×10^6 CD19-CAR T cells in combination with 100 μg Adaptor 3, or 5×10^6 CD19-CAR T cells in combination with 34 μg Adaptor 4, 10 days post treatment. Images are representative of n = 3 mice receiving CAR T cells derived from the same healthy donor. **m** Quantification of CAR T cell distance to the nearest tumor edge of

tumor sections in (**l**). Data are mean values of pooled cells counted from tumor sections of individual mice (n = 3 per group). Significance determined using unpaired Student's t-test (two-tailed, **c-d, k, m**), one-way ANOVA (Sidak's multiple comparisons test, **e, g, h, i**), or Log-rank (Mantel-Cox test, **f, j**). *P* values (**P* < 0.05; ***P* < 0.01; ****P* < 0.001; *****P* < 0.0001; *ns*, not significant).

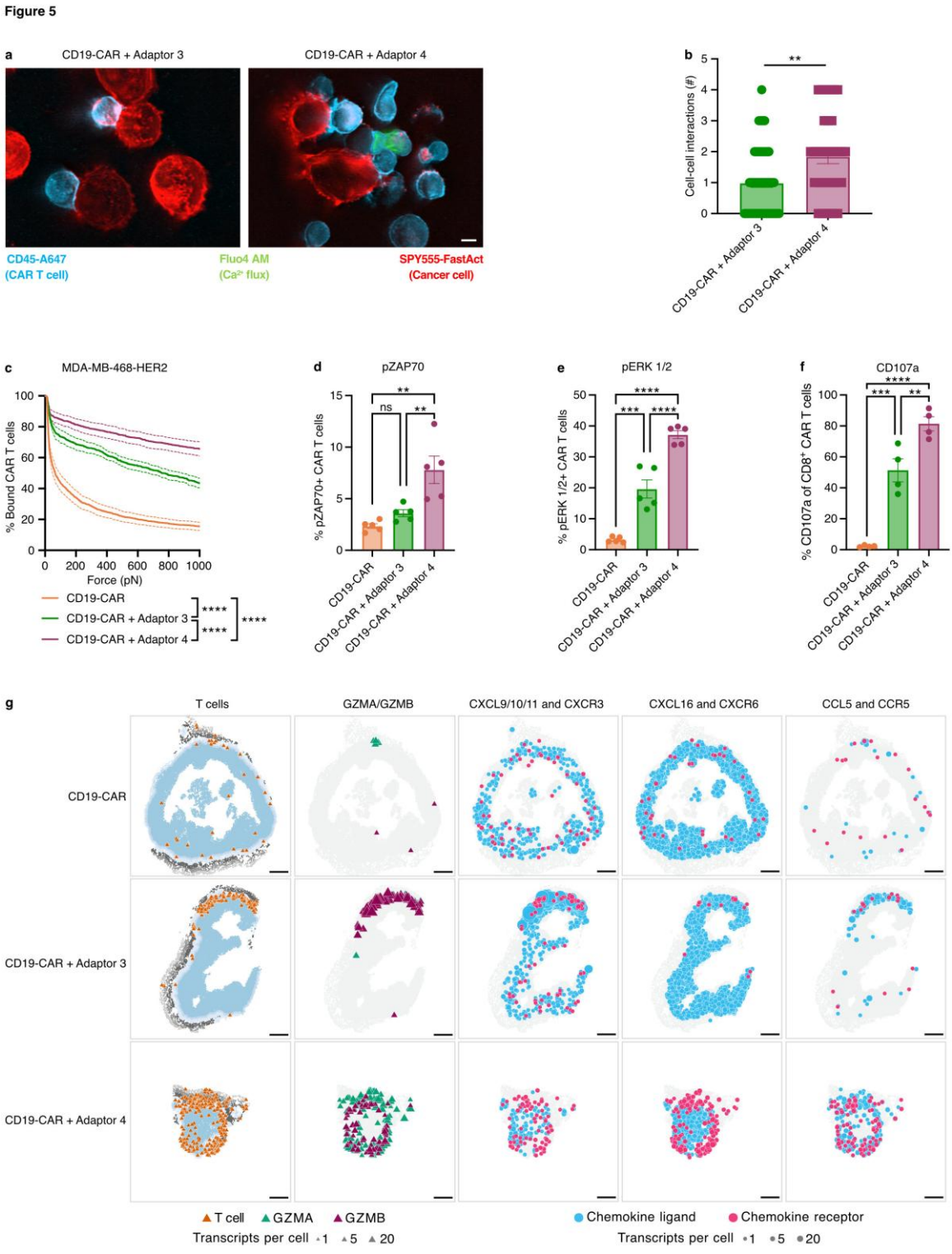


Figure 5. Adaptor 4 induces enhanced CD19-CAR T cells target engagement, signaling, activation and cytotoxicity against MDA-MB-468-HER2 tumors.

a Representative image of synapse formation during CD19-CAR T cell + Adaptor 3 (left) or CD19-CAR T cell + Adaptor 4 (right) interactions with MDA-MB-468-HER2 tumor cells. Scale bar represents 5 μm. **b** Number of interactions quantified between CAR T cells and target

tumor cells. Data represents mean ± SEM of individual cell-cell interactions derived from the same healthy donor within one experiment. **c** Percentage of CD19-CAR T cells remaining bound to MDA-MB-468-HER2 cells, with or without Adaptor, after application of indicated acoustic forces, as measured by z-Movi. Data represent mean ± SEM of pooled values. (CD19-CAR T cells alone, n = 5 independent experiments, technical duplicates or triplicates. Other groups, n = 3 independent experiments, technical duplicates or triplicates.) Percentage of **d** $pZAP70^+$ or **e** pERK $1/2^+$ CD19-CAR T cells when co-incubated with 100 nM Adaptor-bound MDA-MB-468-HER2 cells for 30 min. **d-e** Data are mean ± SEM pooled from two independent experiments involving n = 3 or n = 2 different donors, respectively. **f** Percentage of $CD107a^+$ CAR T cells when co-incubated with MDA-MB-468-HER2 tumor cells with or without Adaptor for 2 hours. Data are mean ± SEM pooled from three independent experiments involving n = 1, n = 1 or n = 2 different donors, respectively. **g** Representative spatial images showing mRNA transcripts in MDA-MB-468-HER2 mammary gland xenograft tumors treated with 5×10^6 CD19-CAR T cells (n = 2), 5×10^6 CD19-CAR T cells in combination with 30 μg Adaptor 3 (n = 2), or 5×10^6 CD19-CAR T cells in combination with 34 μg Adaptor 4 (n = 3). Triangles represent T cell transcripts. Circles represent combined T cell and tumor cell transcripts. Scale bar represents 500 μm. Significance determined using unpaired Student's t-test (two-tailed, **b**) or one-way ANOVA (Tukey's multiple comparisons test, **c-f**). *P* values (**P* < 0.05; ***P* < 0.01; ****P* < 0.001; *****P* < 0.0001; *ns*, not significant).

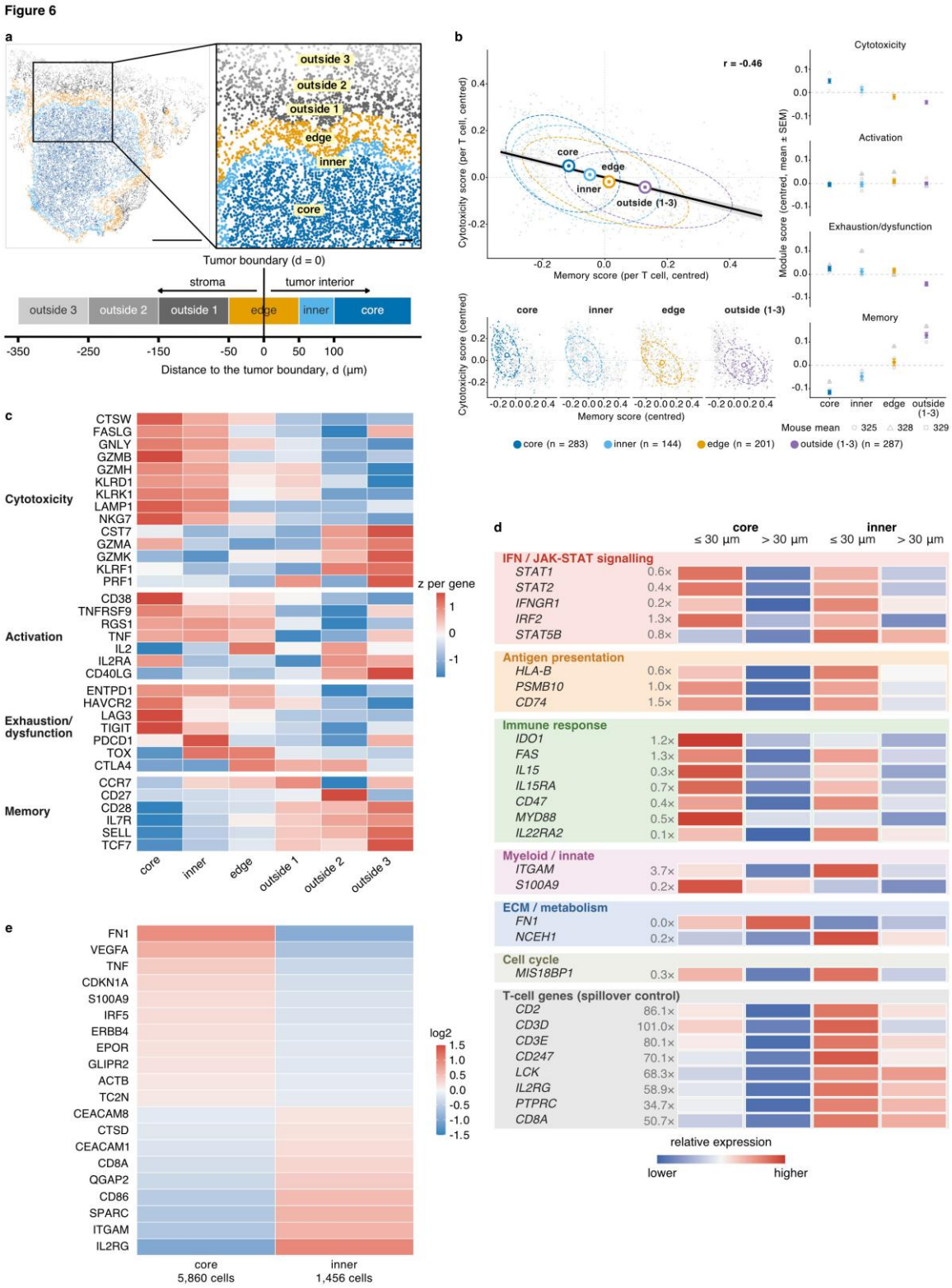


Figure 6. Adaptor 4 induces spatial differentiation of CD19-CAR T cells *in vivo.*

MDA-MB-468-HER2 xenograft tumors were collected from NSG mice treated with 5×10^6 CD19-CAR T cells and 34 µg Adaptor 4, 10 days post treatment (n = 3 mice, all receiving CAR T cells derived from the same donor). **a** Representative spatial image defining different

tumor zones of interest. Scale bar represents 500 μm (top left) or 100 μm (top right). **b** Left: scatter plots showing single cell ssGSEA module scores for memory versus cytotoxicity across different tumor zones (n = 915 T cells, pooled from three mice). Dots represent individual T cells, large rings represent zone centroids, and the black line indicates the least-squares fit over all cells with its 95% confidence band. Sub-panels below break down the data by individual zone, with remaining T cells shown in grey. Right: four T cell expression modules organized by tumor zone. Data are mean ± SEM of pooled T cells within each tumor zone, with open symbols representing the respective means of the three individual mice. **c** Heatmap showing relative gene expression of T cells in the defined tumor zones, grouped into four T cell expression modules. Color represents the z-score of each gene calculated across the six columns. **d** Heatmap showing relative gene expression of tumor cells in the core and inner zones, divided by whether the nearest T cell is within 30 μm. Color represents the z-score of each gene calculated across the four columns. **e** Heatmap showing the top 20 zone-dependent genes in tumor cells, ranked on core vs inner zones. Color represents each gene's $\log_2$ deviation from its combined core and inner zone mean.

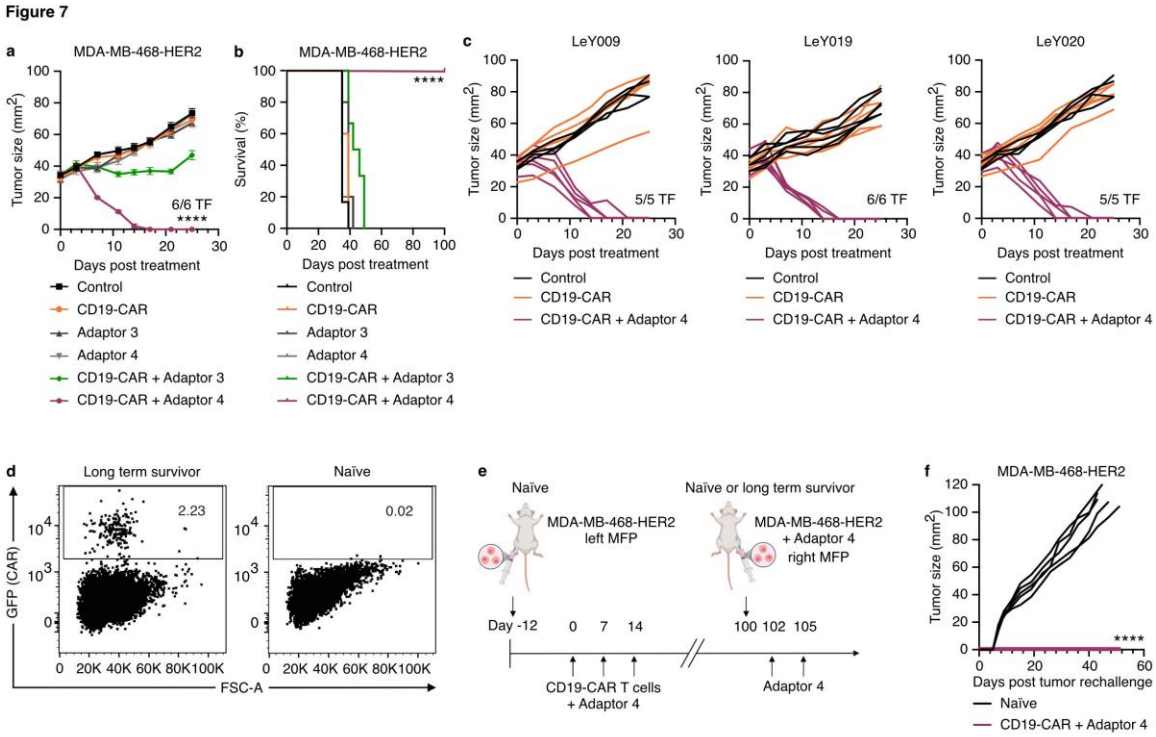
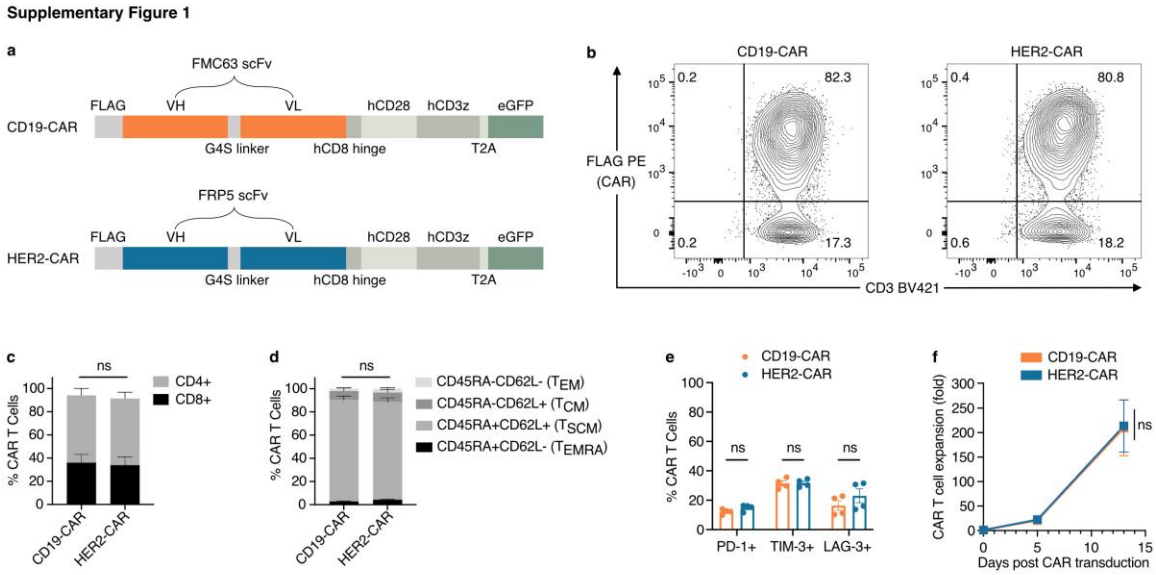


Figure 7. Patient-derived CD19-CAR T cells and Adaptor 4 show durable anti-tumor efficacy and resist tumor rechallenge *in vivo*.

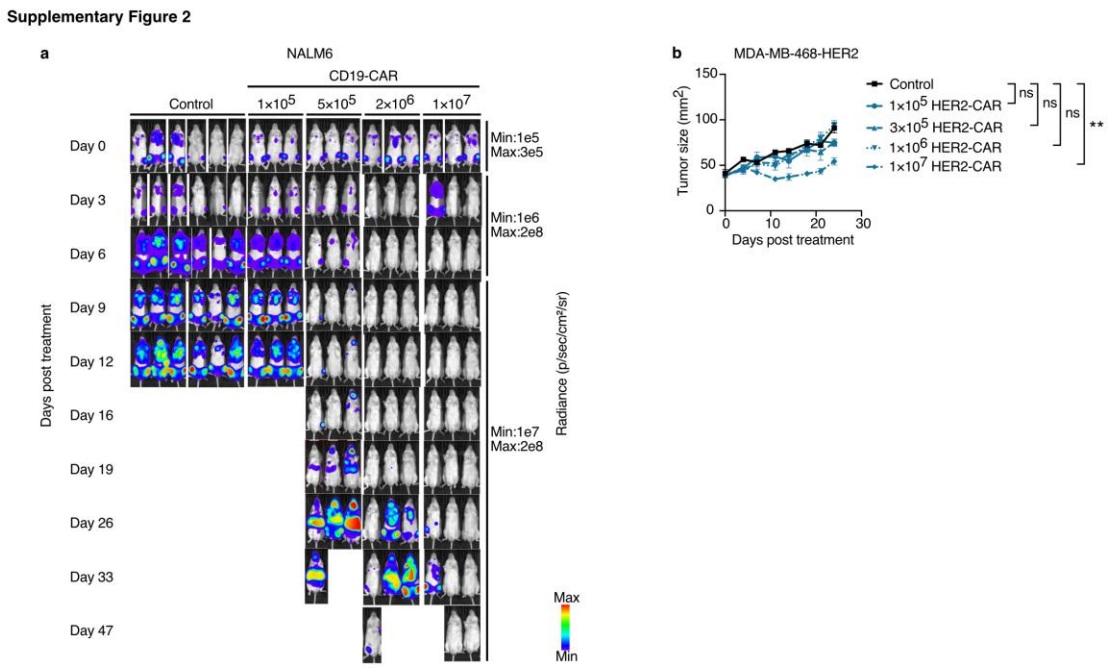
a Tumor growth curves of NSG mice bearing MDA-MB-468-HER2 intra-mammary fat pad tumors receiving no treatment (control), 5×10^6 CD19-CAR T cells, 100 μg Adaptor 3, 34 μg Adaptor 4, 5×10^6 CD19-CAR T cells in combination with 100 μg Adaptor 3, or 5×10^6 CD19-CAR T cells in combination with 34 μg Adaptor 4 (Control, CD19-CAR + Adaptor 3, CD19-CAR + Adaptor 4, n = 6. All other groups, n = 5). CD19-CAR T cells were derived from patient donor LeY019. Data are mean ± SEM. TF, tumor free. **b** Percentage of survival of mice in (**a**). **c** Tumor growth curves of NSG mice bearing MDA-MB-468-HER2 intra-mammary fat pad tumors receiving no treatment, 5×10^6 CD19-CAR T cells with or without 34 μg Adaptor 4 derived from three individual patient donors, LeY009, LeY019, LeY020. Data from the middle graph of control, CD19-CAR (LeY019) and CD19-CAR (LeY019) + Adaptor 4 groups are also shown in (**a**). **d** Representative dot plots of intrasplenic CD19-CAR T cells from naïve NSG mice (left) or from tumor-free mice that received CD19-CAR + Adaptor 4 treatment, 100 days since first treatment. **e** Tumor rechallenge growth curves of naïve NSG mice or tumor-free mice that received CD19-CAR + Adaptor 4 treatment in (**a**), 100 days since first treatment.

Supplementary figures



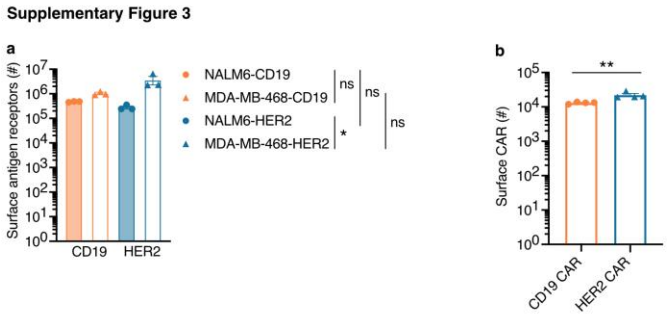
Supplementary Figure 1. CD19- and HER2-CAR T cells display similar resting phenotype and exhibit effector function *in vitro*.

a Schematic overview of the CD19- and HER2-CAR constructs. Flow cytometry analysis of CD19- and HER2-CAR T cells 7 days post CAR transduction, showing **b** representative surface CAR (FLAG) and CD3 expression on CD19- and HER2-CAR T cells, **c** CD4 and CD8 composition, **d** memory subset composition and **e** PD-1, TIM-3 and LAG-3 expression. **f** Fold expansion of bulk CD19- and HER2-CAR T cell populations during *in vitro* culture. **c-f** Data are mean ± SEM (n = 4 different donors). Significance determined using unpaired Student's *t*-test (two-tailed). *P* values (**P* < 0.05; ***P* < 0.01; ****P* < 0.001; *****P* < 0.0001; *ns*, not significant).



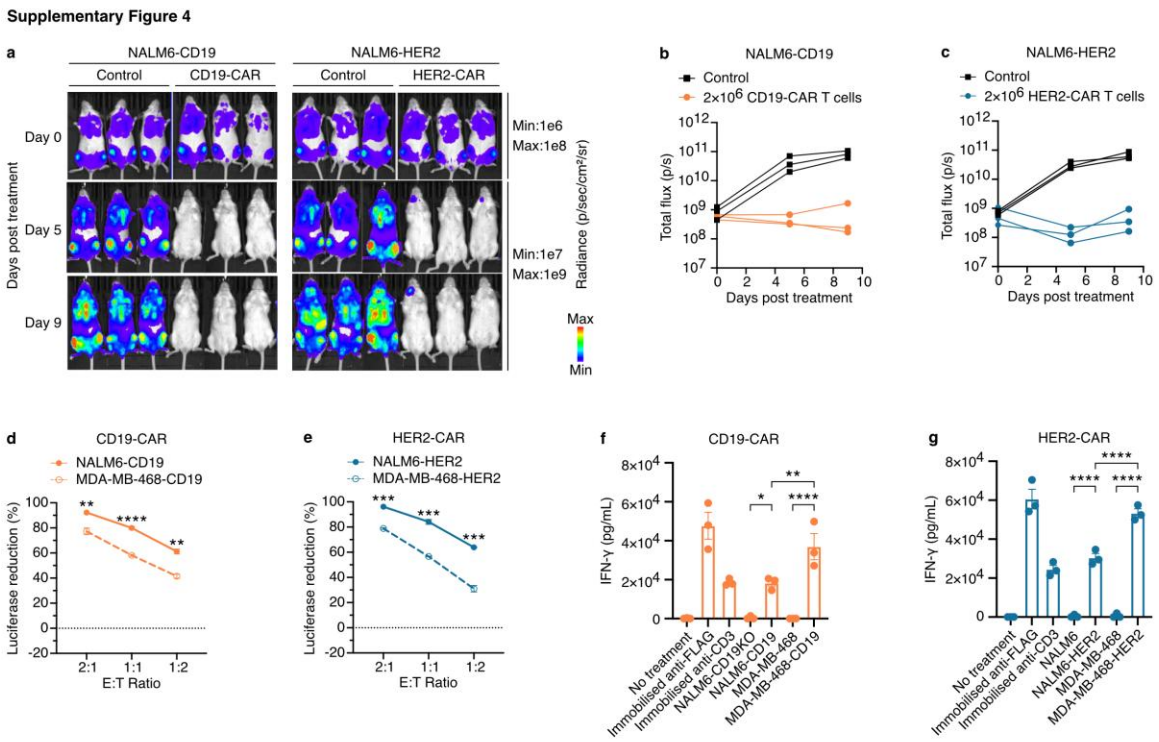
Supplementary Figure 2. Titrating the treatment dose of CD19- and HER2-CAR T cells in NSG xenograft models.

a Bioluminescent image of NSG mice bearing NALM6-luciferase leukemia (no treatment, n=6; all other groups, n = 3 mice receiving CAR T cells derived from the same donor). **b** Tumor sizes of NSG mice bearing MDA-MB-468-HER2 intra-mammary fat pad tumors. Data are mean ± SEM (n = 4 mice receiving CAR T cells derived from the same donor). Significance determined using one-way ANOVA (Dunnett's multiple comparisons test). *P* values (*$P <$ 0.05; **$P < 0.01$; ***$P < 0.001$; ****$P < 0.0001$; *ns*, not significant).



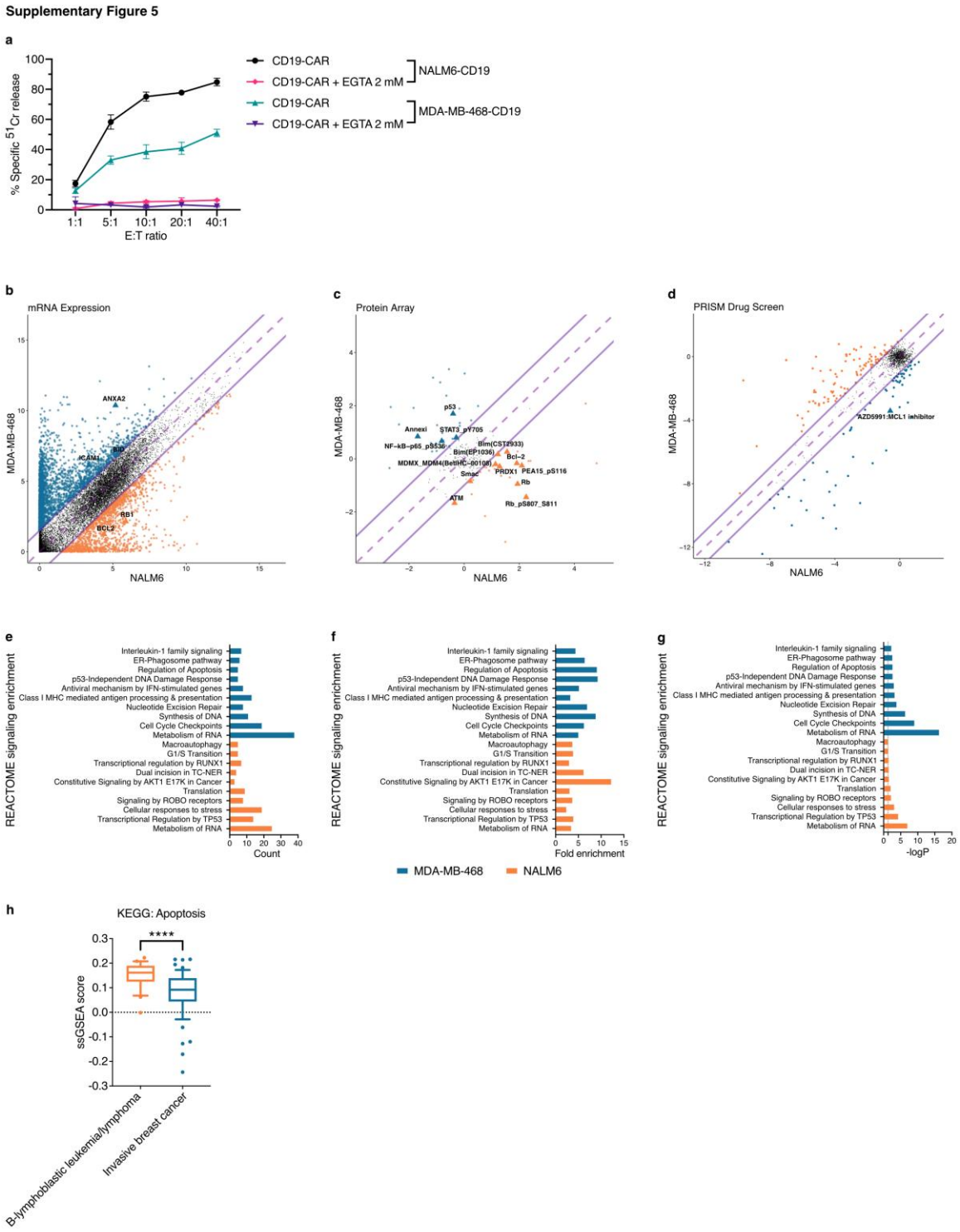
Supplementary Figure 3. Characterizing antigen density and growth of cancer cell lines and CAR density of CAR T cells.

a Flow cytometry analysis quantifying the number of surface antigen receptors on cancer cell lines using Quantum Simply Cellular beads. Data are mean ± SEM (n = 3 independent experiments). **b** Flow cytometry analysis quantifying number of surface CAR molecules on CAR T cells using QuantiBRITE PE beads. Data are mean ± SEM (n = 4 donors). Significance determined using one-way ANOVA (Sidak's multiple comparisons test, **a**) or unpaired Student's *t*-test (two-tailed, **b**). *P* values (*$P < 0.05$; **$P < 0.01$; ***$P < 0.001$; ****$P < 0.0001$; *ns*, not significant).



Supplementary Figure 4. CD19- and HER2-CAR T cells show similar efficacy in leukemia xenograft models and *in vitro*.

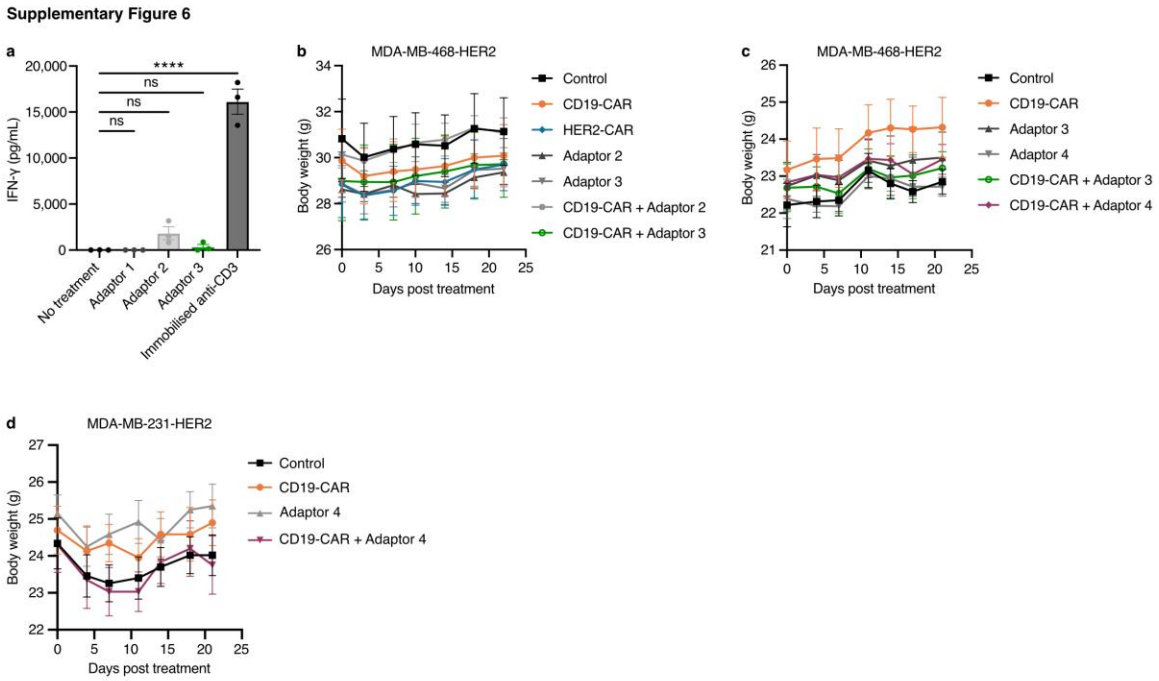
a Bioluminescent image of NSG mice bearing NALM6-CD19-luciferase leukemia (left) or NALM6-HER2-luciferase leukemia (right), (n = 4 per treatment group, all mice received CAR T cells derived from the same donor). **b** Total flux of mice in **a** (left). **c** Total flux of mice in **a** (right). **d** Luciferase reduction of NALM6-CD19 or MDA-MB-468-CD19 cells following overnight co-incubation with CD19-CAR T cells. **e** Luciferase reduction of NALM6-HER2 or MDA-MB-468-HER2 cells following overnight co-incubation with HER2-CAR T cells. **f** IFN-γ production by CD19-CAR T cells after overnight co-incubation alone (no treatment) or with 1 μg immobilized anti-FLAG antibody, 1 μg immobilized anti-CD3 antibody, or indicated tumor cells at 1:1 ratio. **g** IFN-γ production by HER2-CAR T cells after overnight co-incubation alone (no treatment) or with 1 μg immobilized anti-FLAG antibody, 1 μg immobilized anti-CD3 antibody, or indicated tumor cells at 1:1 ratio. Data are representative of three independent experiments involving different healthy donors, shown as mean ± SEM (technical triplicates). Significance determined using unpaired Student's *t*-test (two-tailed, **d-e**) or one-way ANOVA (Sidak's multiple comparisons test, **f-g**). *P* values (*$P < 0.05$; **$P < 0.01$; ***$P < 0.001$; ****$P < 0.0001$; *ns*, not significant).



Supplementary Figure 5. NALM6 cells are more susceptible to apoptosis and CAR T cell mediated killing than MDA-MB-468 cells.

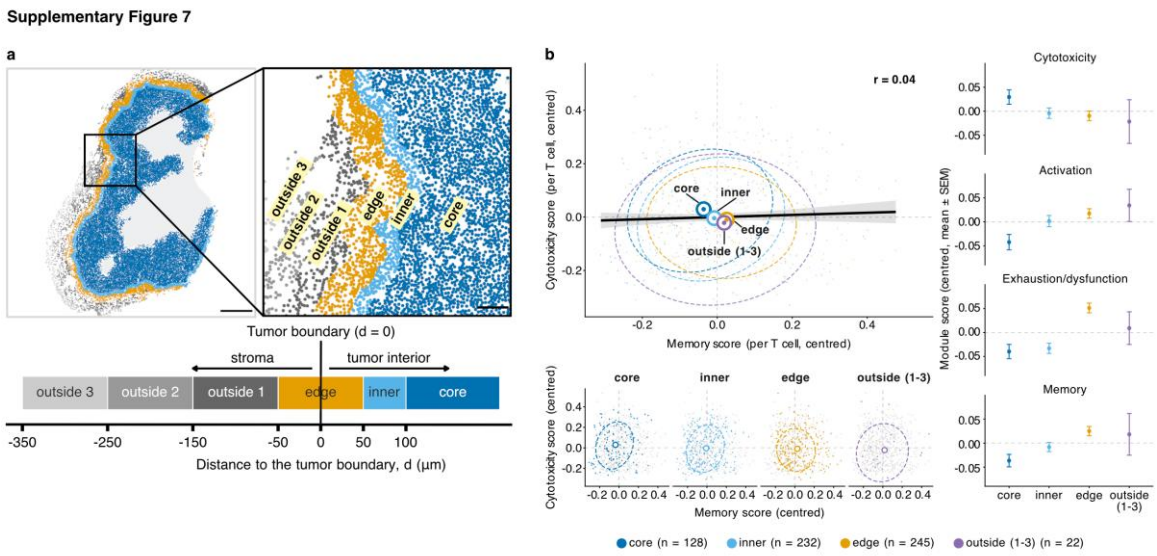
a Specific ^{51}Cr release of NALM6-CD19 or MDA-MB-468-CD19 cells following 4-hour incubation with CD19-CAR T cells, with or without 2 mM EGTA. Data are representative of two independent experiments involving different healthy donors, shown as mean ± SEM (technical triplicates). **b** Scatter plot comparing mRNA expression (transcripts per million,

TPM) of 19,144 genes between MDA-MB-468 and NALM6. X and Y axes represent z scores of mRNA expression. Dashed line represents equal mRNA expression in both cell types. Dots above the upper solid line indicate higher mRNA expression in MDA-MB-468, while dots below the lower solid line indicate higher mRNA expression in NALM6. Triangle dots indicate significantly differentially expressed mRNA related to apoptosis. **c** Scatter plot comparing protein expression detected by 214 antibodies using reverse-phase protein array between MDA-MB-468 and NALM6. X and Y axes represent z scores of protein expression. Dashed line represents equal protein expression in both cell types. Dots above the upper solid line indicate higher protein expression in MDA-MB-468, while dots below the line indicate higher protein expression in NALM6. Triangle dots indicate significantly differentially expressed proteins related to apoptosis. **d** Scatter plot comparing drug sensitivity to inhibitors between MDA-MB-468 and NALM6. X and Y axes represent LFC values. Dashed line represents equal drug sensitivity in both cell types. Lower values indicate higher sensitivity to inhibitors. **e-g** Bar plots depicting the most significantly enriched REACTOME signaling pathways among preferentially essential genes in MDA-MB-468 (blue) and NALM6 cells (orange). Preferentially essential genes are defined as those with gene effect scores less than -1 from RNAi and CRISPR knockout screenings. Top enriched pathways are detailed with gene count (**e**), fold enrichment score (**f**), and p-value (**g**). **h** Box plot of single-sample gene set enrichment analysis (ssGSEA) scores for the Kyoto Encyclopedia of Genes and Genomes (KEGG) apoptosis pathway in B-lymphoblastic leukemia/lymphoma (n = 24) and invasive breast cancer cells (n = 58). Significance determined using unpaired Student's *t*-test (two-tailed, **h**). *P* values (*$P < 0.05$; **$P < 0.01$; ***$P < 0.001$; ****$P < 0.0001$; *ns*, not significant). mRNA, protein, drug sensitivity and ssGSEA data were retrieved from DepMap (https://depmap.org/portal/).



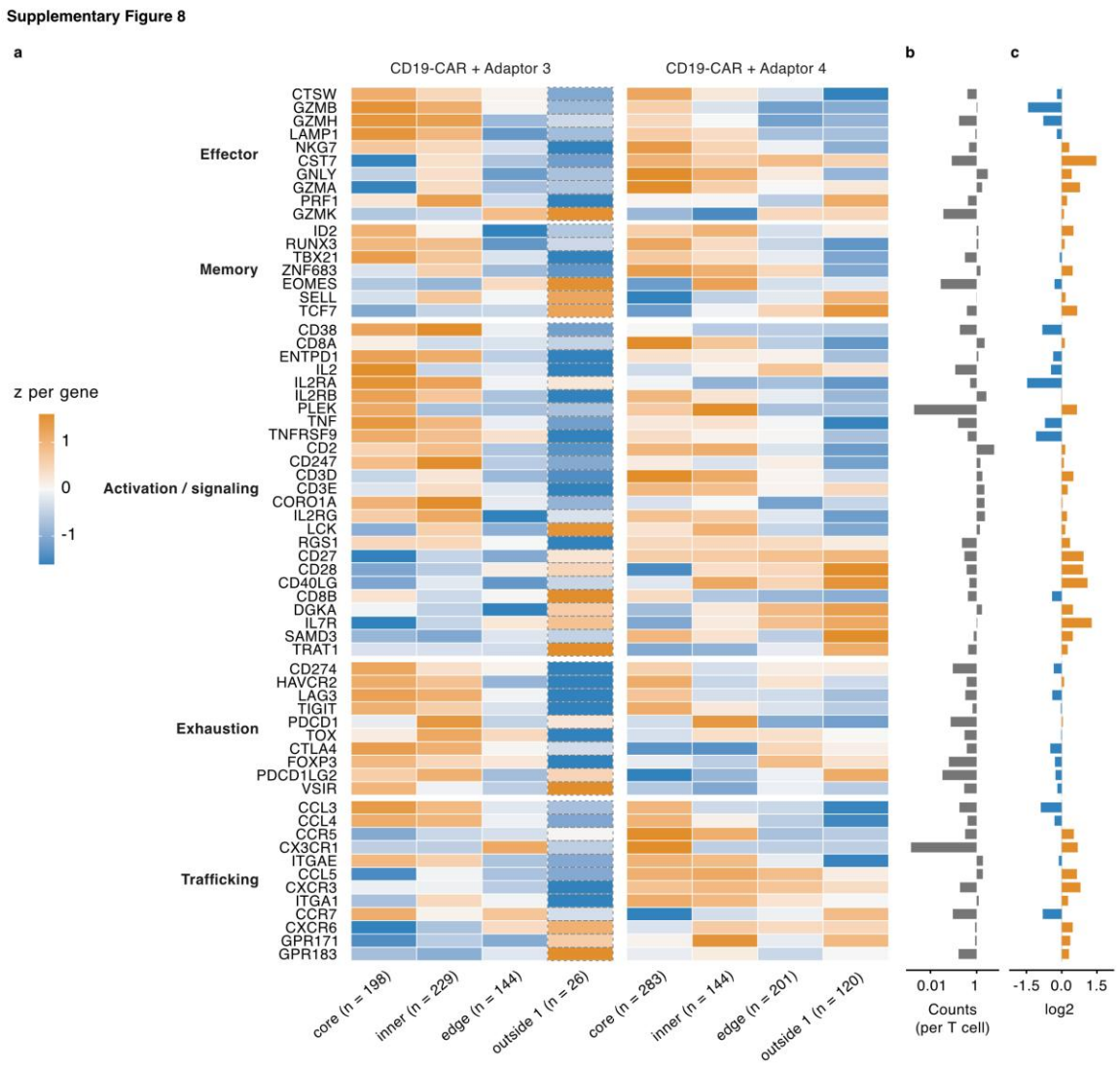
Supplementary Figure 6. Adaptors do not induce antigen-independent CD19-CAR T cell activation in vitro nor detectable body weight loss *in vivo*.

a IFN-γ production by CD19-CAR T cells after overnight co-incubation in media only (no treatment) or with 10 nM Adaptor 1 or 2, 5 nM Adaptor 3 or with 1 μg immobilized anti-CD3 antibody. Data are representative of three independent experiments with different healthy donors, shown as mean ± SEM (technical triplicates). **b** Body weight of mice in **Figure 3g**. **c** Body weight of mice in **Figure 4e**. **d** Body weight of mice in **Figure 4i**. Significance determined using one-way ANOVA (Dunnett's multiple comparisons test, **a**). *P* values (*$P < 0.05$; **$P < 0.01$; ***$P < 0.001$; ****$P < 0.0001$; *ns*, not significant).



Supplementary Figure 7. Adaptor 3 does not induce spatial differentiation of CD19-CAR T cells *in vivo.*

MDA-MB-468-HER2 xenograft tumors were collected from NSG mice treated with 5×10^6 CD19-CAR T cells and 30 µg Adaptor 3, 5 days post treatment (n = 2). **a** Representative spatial image defining different tumor zones of interest. Scale bar represents 500 µm (top left) or 100 µm (top right). **b** Left: scatter plots showing single cell ssGSEA module scores for memory versus cytotoxicity across different tumor zones (n = 627 T cells, pooled from two mice). Dots represent individual T cells, large rings represent zone centroids, and the black line indicates the least-squares fit over all cells with its 95% confidence band. Sub-panels below break down the data by individual zone, with remaining T cells shown in grey. Right: four T cell expression modules organized by tumor zone. Data are mean ± SEM of pooled T cells within each tumor zone.



Supplementary Figure 8. Adaptor 4 enhances CD19-CAR T cell functionality relative to Adaptor 3 *in vivo.*

MDA-MB-468-HER2 xenograft tumors were collected from NSG mice treated with 5×10^6 CD19-CAR T cells and 100 µg Adaptor 3 (n = 3) or 5×10^6 CD19-CAR T cells and 34 µg Adaptor 4 (n = 3). Heatmap showing **a** z-scores per gene across tumor zones, **b** transcript counts per T cell and **c** log2 fold change in CD19-CAR + Adaptor 4 treated samples relative to CD19-CAR + Adaptor 3 treated samples of pooled T cells within defined spatial zones of the same treatment group. The number of pooled T cells within each region is indicated in brackets. The CD19-CAR + Adaptor 3 outside 1 group is highlighted by a dashed outline due to the low number of T cells detected and analyzed.

Supplementary Files

This is a list of supplementary files associated with this preprint. Click to download.

- SupplementaryMovie2Adaptor3synapseformation.mp4
- SupplementaryMovie1Adaptor4synapseformation.mp4